ANL/NE-15/19

Experimental Results for Direct Electron Irradiation of a Uranyl Sulfate Solution: Bubble Formation and Thermal Hydraulics Studies

Nuclear Engineering Division

ANL/NE-15/19

Experimental Results for Direct Electron Irradiation of a Uranyl Sulfate Solution: Bubble Formation and Thermal Hydraulics Studies

by
Sergey Chemerisov, Roman Gromov, Vakho Makarashvili, Thad Heltemes, Zaijing Sun, Kent Wardle, James Bailey, Dominique Stepinski, James Jerden, and George F. Vandegrift
Nuclear Engineering Division, Argonne National Laboratory

January 30, 2015

CONTENTS

FIGURES

FIGURES (Cont.)

FIGURES (Cont.)

TABLES

EXPERIMENTAL RESULTS FOR DIRECT ELECTRON IRRADIATION OF A URANYL SULFATE SOLUTION: BUBBLE FORMATION AND THERMAL HYDRAULICS STUDIES

ABSTRACT

In support of the development of accelerator-driven production of fission product Mo-99 as proposed by SHINE Medical Technologies, a 35 MeV electron linac was used to irradiate depleted-uranium (DU) uranyl sulfate dissolved in pH 1 sulfuric acid at average power densities of 6 kW, 12 kW, and 15 kW. During these irradiations, gas bubbles were generated in the solution due to the radiolytic decomposition of water molecules in the solution. Multiple video cameras were used to record the behavior of bubble generation and transport in the solution. Seven six-channel thermocouples were used to record temperature gradients in the solution from self-heating. Measurements of hydrogen and oxygen concentrations in a helium sweep gas were recorded by a gas chromatograph to estimate production rates during irradiation. These data are being used to validate a computational fluid dynamics (CFD) model of the experiment that includes multiphase flow and a custom bubble injection model for the solution region.

1 INTRODUCTION

SHINE Medical Technologies is planning to use neutron-induced fission in a subcritical low-enriched-uranium uranyl-sulfate target solution for production of ^{99}Mo [1, 2]. During this operation, the solution will undergo self-heating due to fissioning in the solution, radiolytic decomposition of the water in the solution, and circulation due to thermal gradients generated in the solution, which is cooled by cooling tubes running through the annulus and from cooling outside the annulus. Because the formation of the radiolysis-induced bubbles (H_2 and O_2) and their size and dynamics will impact the operational parameters of the liquid target, an understanding of bubble behavior is critical for the ability to predict the behavior of the target solution during this operation. It is also important to be able to predict the thermal gradients and the circulation in the vessel.

In this experiment, we used the electron beam of a linear accelerator to irradiate a solution volume (geometrically similar to a sector of the SHINE annular solution vessel) to study (1) radiolytic-bubble formation, size, and behavior and (2) thermal hydraulics. The design and fabrication of the apparatus have been described elsewhere [3, 4]. Further details of the apparatus and its operation are also included in this report. Figures 1 and 2 are schematics of the "Bubble-Experiment Apparatus." Figures 3–5 are photographs of the apparatus as set up.

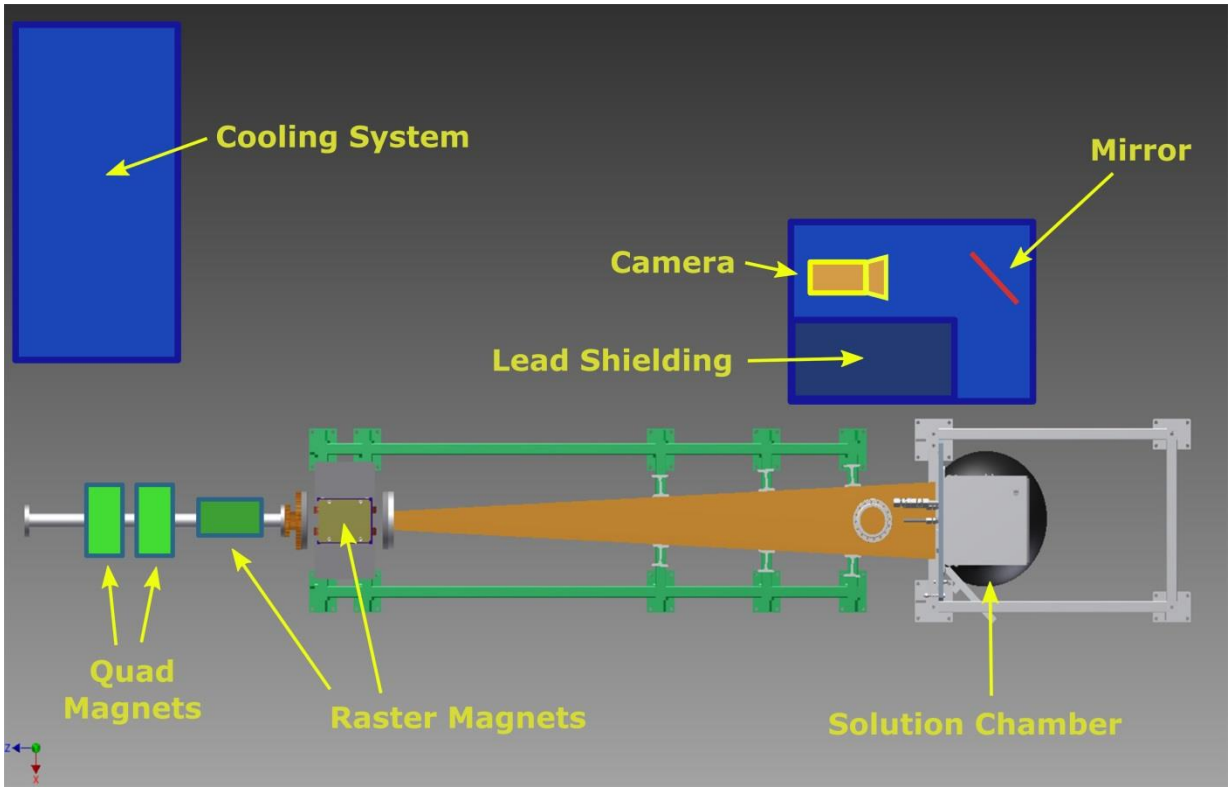

FIGURE 1 Major Elements of the Bubble-Experiment Apparatus

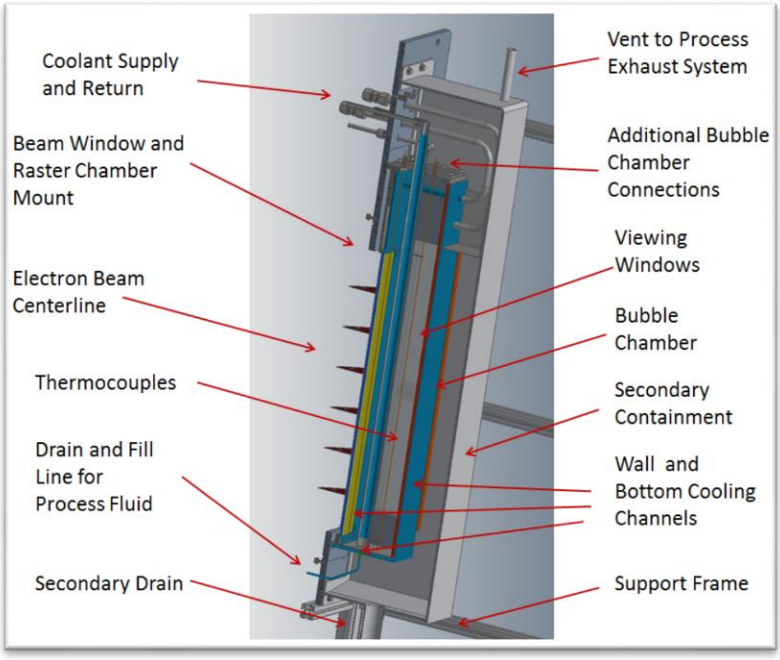

FIGURE 2 Schematic of the Bubble-Experiment Apparatus —Details of Irradiation Vessel

This report describes the experiments and provides experimental data obtained from these experiments. Experimental results obtained in this task will be compared with simulations to fine-tune computer models. A future report will provide analyses of the data and compare the results to fluid-dynamics modelling.

Because the solution will undergo radiolytic decomposition from electrons slowing down in the liquid, we were able to study bubble formation and dynamics and effects of convection and temperature on bubble behavior. While data on radiolytic gas formation is being collected in mini-SHINE experiments [5–7], data for bubble-formation dynamics in phase-2 of the mini-SHINE experiments will be limited due to the complexity of the optical setup for the extremely high radiation fields in the fissioning solution. Utilization of the direct electron beam irradiation allows volumetric heating of a large solution volume and simplifies simultaneous observation of the bubble dynamics with thermal-hydraulic data collection.

Irradiations were conducted by using a 35 MeV electron beam from the high-power linear accelerator. This range of electron-beam energy translates into 15 cm of an average path length of electrons in water (Continuous Slowing Down Approximation, CDMA range [8]), so we can use a large solution volume to study convective behavior resembling the bulk solution. The electron beam was raster-scanned and focused in such a way that almost all of the volume of the 15-cm × 15-cm × 80-cm solution was homogeneously heated. The total electron-beam power was between 3 kW and 15 kW, which will yield an average power density in solution over a range of 0.03–0.45 kW/L. This power was uniformly distributed in the solution in the direction of the beam due to the low linear energy transfer (LET) of the high energy electrons. The

FIGURE 3 Photograph of the Assembled Bubble-Experiment Vessel

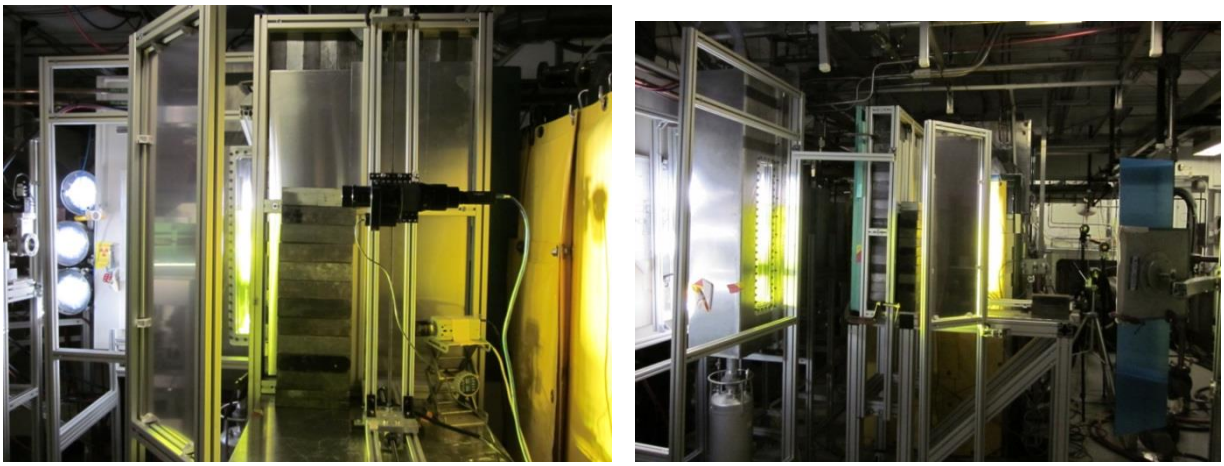

View from beam side **View from downstream side**

FIGURE 4 Bubble-Experiment Vessel with Mirrors, Backlights, and Cameras in Place. Photos were taken from the front and back, parallel to the beamline.

FIGURE 5 Bubble Vessel Attached to Beamline Prior to Completing Installation

electron beam was scanned over the face of the beam window with 1 Hz frequency to ensure uniform power distribution within the convection time constant of the solution [3].

The solution volume was actively cooled on the front and back surfaces and by a central tube to mimic the geometry of the proposed SHINE solution vessel. Sides of the irradiation volume were constructed from optical quartz, so bubble formation and propagation could be observed using optical cameras. Also, 42 thermocouples were inserted into and above the solution to map its thermal profiles.

Radiolysis of water has been very well studied and even without dissolved salts and gases in the solution, it has been shown that 50 elementary reactions and their rate constants are required to adequately describe radiolysis of water and its subsequent relaxation. Further complications are added by dissolved species (gases and salts), which can react with hydrated electrons, radicals, intermediates, and molecular species. These reactions affect both the generation rate of hydrogen and hydrogen peroxide and the decomposition of hydrogen peroxide. Hydrogen peroxide can be oxidized to oxygen, reduced to water, or it can self-destruct into water and oxygen [9]. Another complication is that such high concentrations of solutes will deposit considerable energy in the solution. According to literature data, gas generation due to electron radiolysis is expected to be one-fourth that due to fission fragments [8], but we varied the power density in the solution to make up for the difference in the generation rate. We combined bubble dynamic observation with gas-generation measurements using a gas chromatography to establish a correlation between bubble dynamics and the time required for establishing the steady-state

concentrations and onset of oxygen formation. We irradiated water as well as a uranium-salt solution to study the thermal hydraulics of the system.

Before the final design of the bubble experiment, preliminary testing of concepts and equipment was performed in a series of experiments at the Van de Graaff (VDG) generator. These studies can be found in a separate report [10].

The following sections present a summary of the data collected during the experiments and the planned efforts to analyze the results and compare them to computer modelling results that describe the hydraulic and thermal dynamics of the system.

2 EXPERIMENT DESCRIPTION

2.1 TEMPERATURE PROFILING THERMOCOUPLES

The solution was instrumented with seven six-channel thermocouples around the central cooling channel, as shown in Figure 6. Thermocouple channels 1–5 were in the solution and channel 6 was in the gas head space above the solution. In addition to these thermocouple assemblies, a thermocouple was affixed to the back of the primary containment wall and another was hanging in the secondary containment atmosphere to measure the atmosphere temperature. The arrangement of the thermocouple wires and central cooling channel are shown in Figure 6. A LabVIEW-based data-acquisition system was used to collect the signals from all thermocouples.

2.2 COOLING SYSTEM

The cooling system for the experiment is designed to have sufficient capacity to remove 20 kW of heat. A cooling-water pump is sized to provide 50 gpm (189 L/m) of water flow at up to 50 psig (345 Pascal) pressure. The cooling system has an all-welded design. All components are stainless steel and equipped with a mixed-bed deionizer to remove possible contaminants from the cooling water. The head space of the make-up tank is purged by air and is vented through the HEPA-filter-equipped exhaust system to prevent hydrogen buildup. All elements of

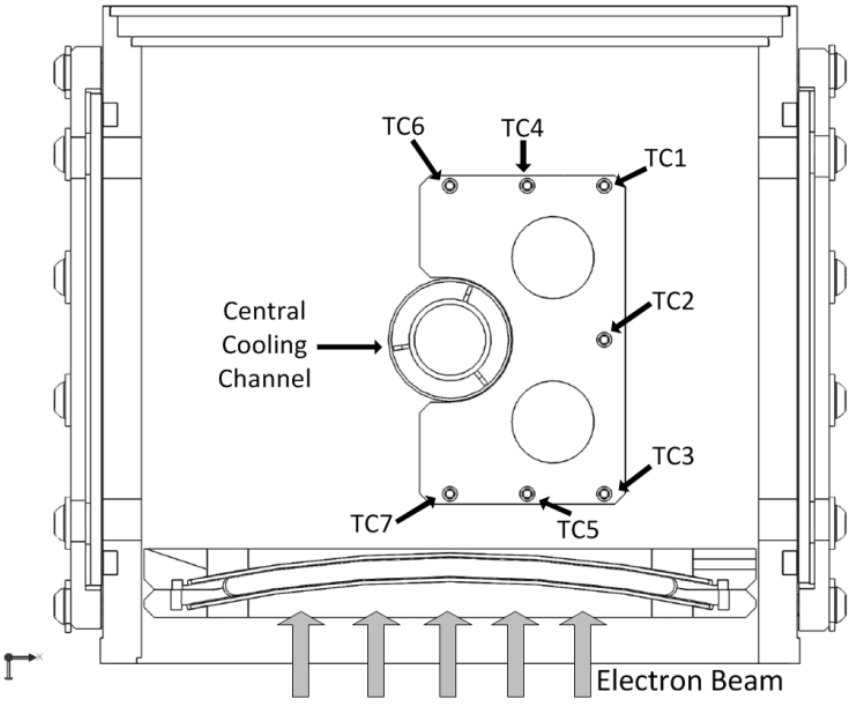

FIGURE 6 Cross Section of the Experiment's Primary Containment Vessel

the cooling system that are not welded are located inside an enclosure to prevent the spread of suspect coolant water to the environment. This enclosure is also connected to the exhaust system. The cooling system enclosure is shown in Figure 7.

2.3 BEAM HANDLING SYSTEM

The experimental set up for vessel irradiation requires an even beam deposition over the target surface. To comply with this requirement, a rastering system was designed and installed on the beamline. The concept is to use fast-oscillating low-induction bending magnets so the beam will cover as much of the front target area as possible. To get better uniformity of the power deposition, the beam is defocused in one or both transverse directions. The beam profile forming system consists of two parts: defocusing and rastering (Figure 8).

FIGURE 7 Cooling System Enclosure

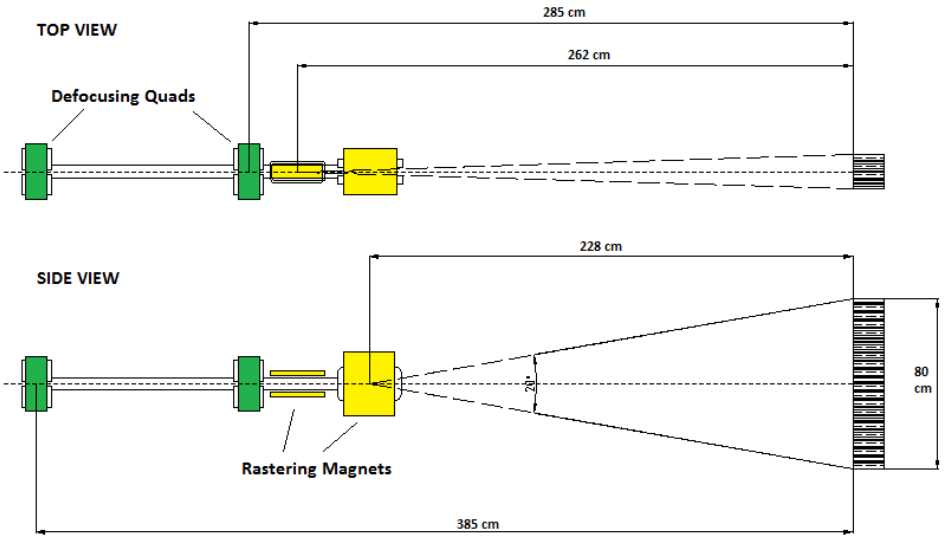

FIGURE 8 Beam Profile Forming System Layout

Defocusing sub-system: The initial accelerated electron beam has a small transverse size, about 3 x 5 mm. To increase the beam size in the horizontal and vertical directions, the last quad doublet was used as a defocusing element. This was achieved by over-focusing of the beam in both directions, which increases the spot size on the target to about 30 x 40 mm. Further defocusing was not applied, because this would lead to a dramatic decrease in the beam uniformity and loss of electrons due to energy spread.

Rastering sub-system: The defocused beam was directed to the target front window through the raster system, which consists of two bending magnets with the ability to bend an electron beam in two directions: ±10° in the vertical direction and ±1° in the horizontal direction. Their power supplies were controlled by an external programmable pulse forming generator with variable frequency (Figure 9). Two different rastering patterns were tested with the target: first, rastering the beam on the rectangular shape, and second, rastering the beam with the "∞"-shape. Due to its more uniform power-deposition distribution to the target volume (Figure 10), the first pattern was used as the primary operational mode for the experiment.

2.4 CAMERA/LIGHTING SETUP

The task of quantitatively capturing moving sub-millimeter bubbles in solution is non-trivial. When this is to be done in an operating solution reactor with a radiation field requiring a significant standoff distance the challenge is all the more difficult. Thus, careful consideration of lighting, mirrors, lenses, and cameras was taken and based on the best information available regarding the expected characteristics of the bubbles, and preliminary experiments undertaken at the Van de Graaff facility in early Fiscal Year 2014 [10], a configuration that could provide the necessary imaging performance was selected. While the size and velocity of the bubbles was not known *a priori*, it was thought to be in the ~1 mm range and having velocities of several cm/s according to the observation of the micro-bubble experiments at the Van de Graaff facility. Thus,

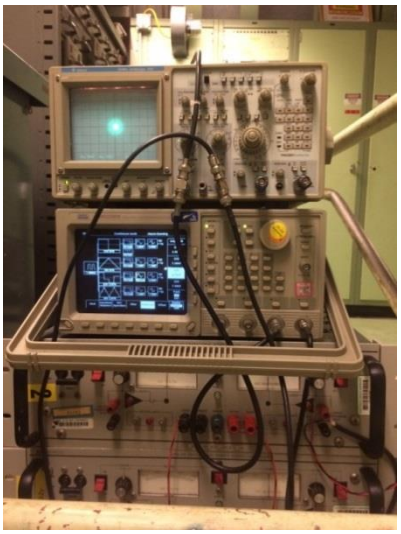

FIGURE 9 Programmed Pulse Generator and Power Supplies

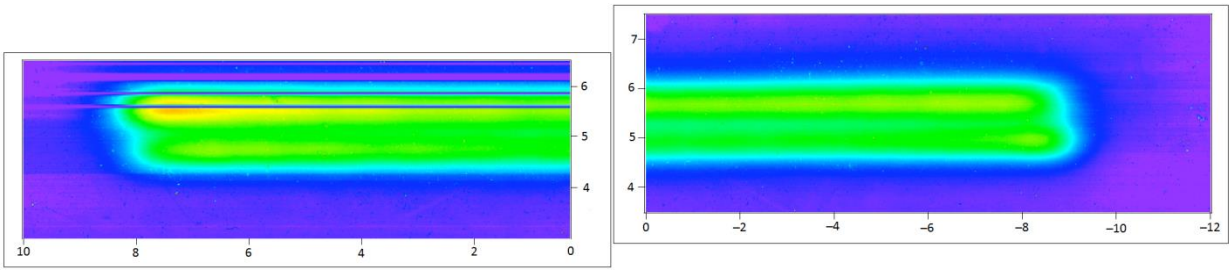

FIGURE 10 Rectangular Beam Profile Sample Obtained from Plexiglas Film Irradiation. Dimensions are given in inches. The x-axis in this figure is the vertical extent of the beam (positive up) and the y-axis is the horizontal extent of the beam from left to right as facing the Bubble Chamber primary.

for velocimetry, a camera frame rate greater than 100 frames/s was considered necessary. Based on this assumption, a monochromatic camera having a gray scale resolution of 1920 x 1200 pixels with a global shutter and capable of 162 frames/s enabled by a connection over SuperSpeed USB 3.0 was used (Point Grey Grasshopper model GS3-U3-23S6M-C). This camera was combined with a long-range telecentric lens system from Infinity Photo-Optics USA (K1 CentriMax with MX-LR objective, 2 NTX-2x tube adapters, and remote focusing motor) to provide adequate magnification at a stand-off distance of approximately 1.5 m. The lens/camera was mounted on a two-axis traverse stage (controlled by a custom LabVIEW interface) with a linear range of nearly 80 cm to allow access to the entire area of the imaging window. The traverse system was mounted on a custom table which held a wall of 4” thick lead (for x-ray shielding) and 2” of polyethylene (for neutron shielding) to protect the lens and cameras. A first surface mirror (aluminum on glass) was oriented at 45 degrees in front of the camera to give a

precise image of the bubble chamber window with the camera aligned parallel with the beam axis. A second set of mirrors (polished stainless steel) was used to direct the light through the window on the opposite side of the chamber and provide sufficient backlighting for bubble imaging. Light was provided by a vertical stack of three, 250 W LED stage spotlights (Altman Phoenix Profile LED Spotlight, model PHX2-5600K-10-B).

An additional color camera with higher resolution but lower frame rate (Point Grey Flea model FL3-U3-88S2C-C, 4096 x 2160, 21 fps, rolling shutter, USB 3.0) was used to view the full length of the chamber window. Given the challenges that were encountered in preliminary tests with the stability of the USB 3.0 connection over the long active repeater cables, an additional set of 3 IP cameras (each a 2MP VIVOTEK IP7160 connected over Ethernet), was required and positioned so as to view the top, middle, and bottom of the liquid region of the chamber. IP cameras can record the video continuously over the network in 3GP format through a VAST/ST7501 program installed on a local computer. For better shielding, these four cameras were positioned behind the gas collection system, which already has lead walls against the beamline. Figure 11 shows a snapshot of the setup.

While a sufficient number of images were obtained to determine the bubble size and estimate the velocity of the bubbles and bulk liquid, data collection was only possible at a few points, given the delays caused by the instability of the USB 3.0 connection to the cameras. Additionally, quantitative bubble data were obtained only for the 6 kW and 12 kW beam conditions. At the 15 kW power setting, the lens' remote focusing mechanism had become inoperable. The clarity of the final images was also limited due to the necessity of two sets of windows (on the primary and secondary containment) creating a greater chance for reflection.

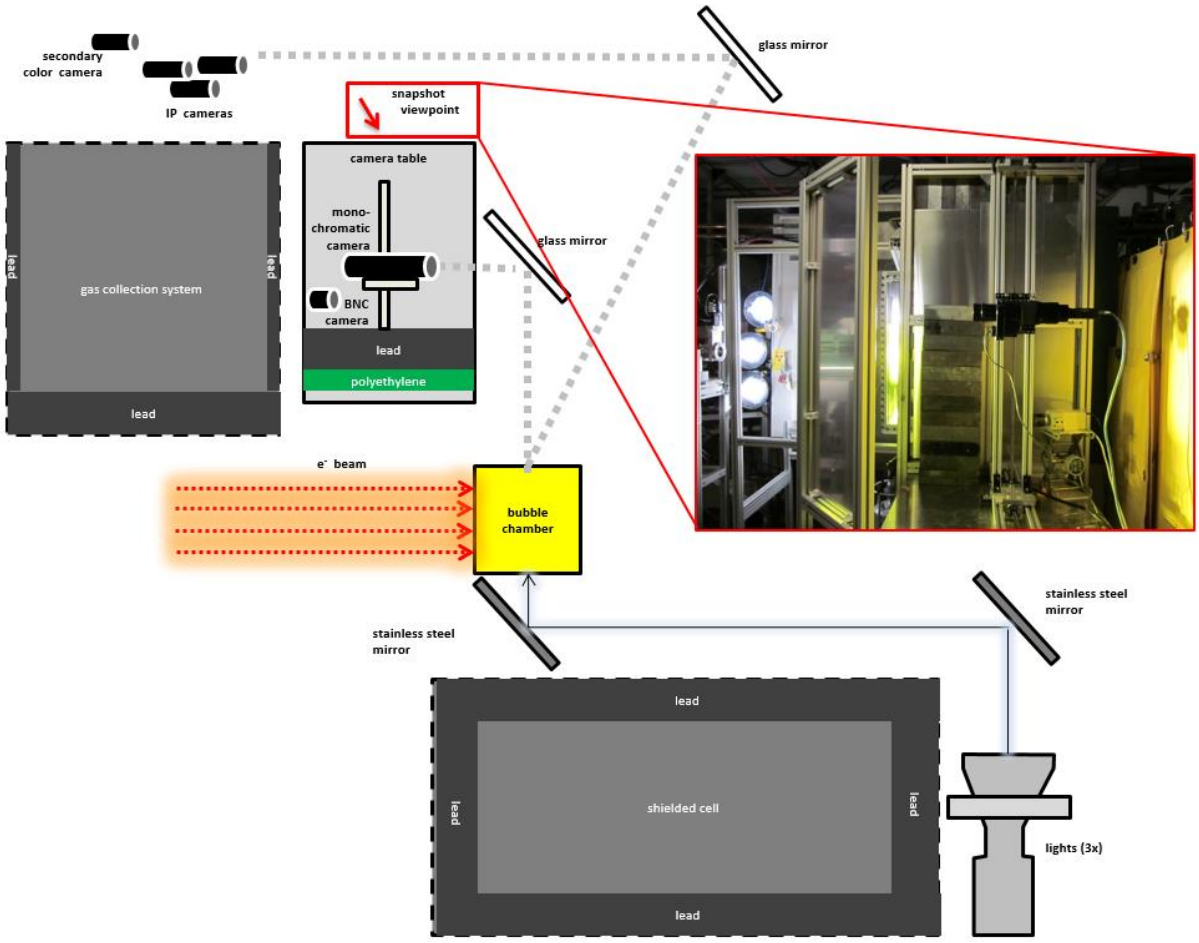

FIGURE 11 Layout of the Imaging Setup with the Primary Bubble Imaging Camera System Mounted Behind the Wall of Lead Shielding Bricks as Shown in the Inset Snapshot. The viewpoint of the snapshot is shown in the diagram. The mirror on the imaging side is seen in the left foreground and the three 250 W LED spotlights can be seen in the background at the left.

3 RESULTS AND DISCUSSION

3.1 COOLING SYSTEM PERFORMANCE

Bubble formation experiments were performed in two phases. The first phase was done with water in the primary chamber, while the second phase was performed with 140 g-U/L uranyl sulfate as the target solution. The cooling system was not fully instrumented with thermocouples during the water irradiations. There were only two thermocouples—one was stuck to the body of the secondary aluminum chamber and the other one was hanging in the air, close to the chamber. Temperature readings of these two thermocouples during the water irradiations are presented in Figure 12.

Four more thermocouples where added to the cooling system for the uranyl-sulfate irradiations. These thermocouples were the chiller inlet and outlet, the pump inlet, and the heat exchanger outlet. The cooling-system thermal-performance during uranyl sulfate irradiations is shown in Figure 13. There were three irradiation campaigns for uranyl sulfate—one short (a) and two long (b) and (c) irradiations.

Based on the collected temperature data, the cooling system performed as designed and expected. The chiller inlet temperature was nearly constant, varying between 13–14ºC, while the other five thermocouples tracked thermal loads from the electron beam as various power levels were executed.

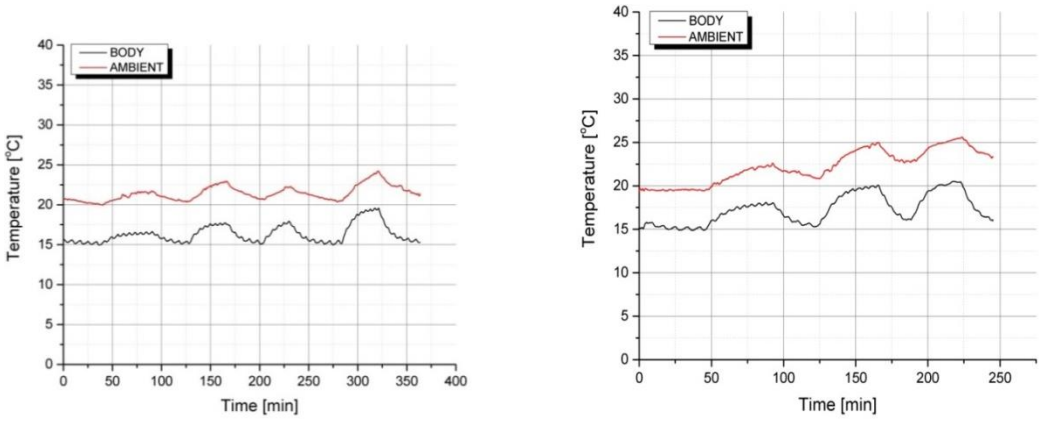

(a) **(b)**

FIGURE 12 Secondary Chamber Body and Ambient Temperature Measurements during the Water Irradiations: (a) First Water Irradiation: 3 and 6 kW Unrastered Beam followed by 6 and 10 kW Rastered Beam, (b) Second Water Irradiation: Rastered Beam at 6, 10, and 12 kW

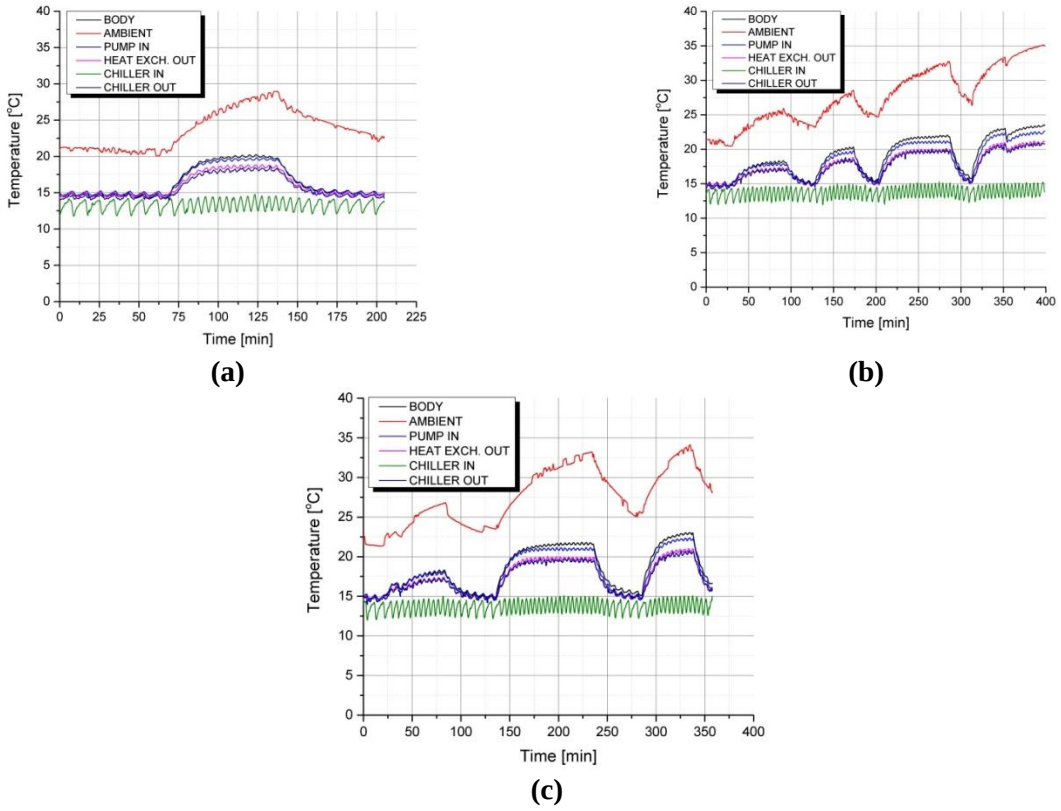

FIGURE 13 Cooling System Performance during the Uranyl Sulfate Irradiations: (a) Short irradiation at 10 kW, (b) First Long Irradiation—6, 10, 12, and 15 kW, and (c) Second Long Irradiation—6, 12 and 15 kW

3.2 TEMPERATURE DISTRIBUTIONS IN THE TARGET-VESSEL TANK

Seven thermocouple rods (numbered TC1 through TC7) were inserted in the target solution vessel at various locations; see Figure 6 for the thermocouple layout. There were six measurement points on each rod numbered 1 through 6, starting from the bottom. The first five points were inside the solution, while the sixth one was above the solution in the head space of the target vessel. So there was a total of 42 temperature measurements—35 inside the target solution and 7 above the solution. Temperature data were recorded for both phases of the experiment, water, and uranyl-sulfate irradiations.

3.3 WATER IRRADIATIONS

Temperature distribution data for the first and second 20 L water irradiations are shown in Figures 14 and 15, respectively. The first water irradiation started with an unrastered circular beam at 3 kW and then increased to 6 kW. After this, the beam rastering was turned on at 6 kW followed by 10 kW. The second irradiation was performed with a rastered beam at progressively higher power—6, 10 and 12 kW. Each bump in the data corresponds to turning the beam on and off at different power levels. Figure 14 shows a clear difference between unrastered and rastered

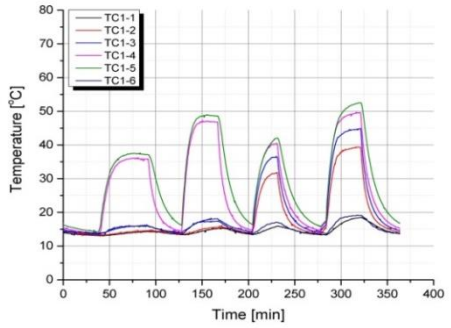

(a) TC1

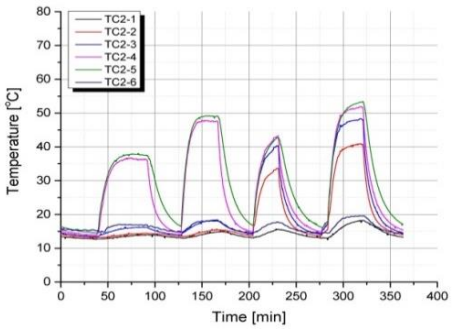

(b) TC2

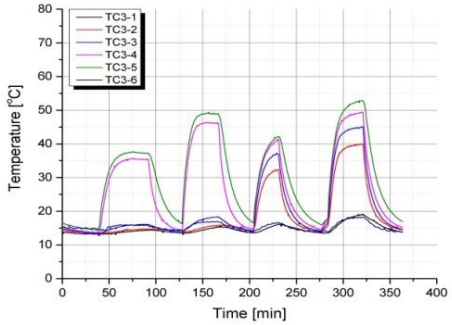

(c) TC3

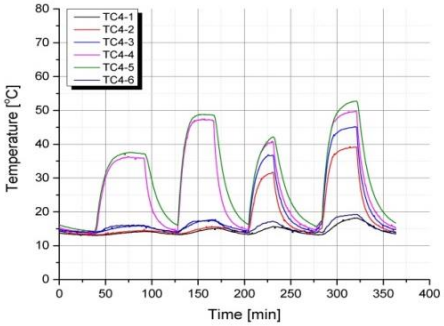

(d) TC4

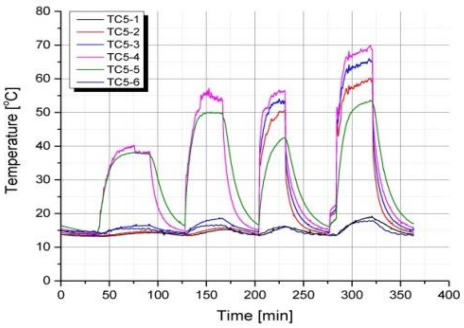

(e) TC5

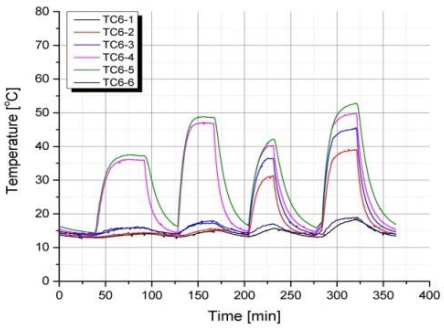

(f) TC6

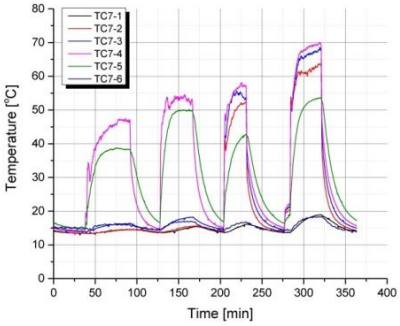

(g) TC7

FIGURE 14 Temperature Distributions for each TC Set for the First Water Irradiation Started with an Unrastered Beam at 3 and 6 kW, Followed by a Rastered Beam at 6 and 10 kW. TC5 and TC7 were heated up directly by the beam and do not represent the water temperatures.

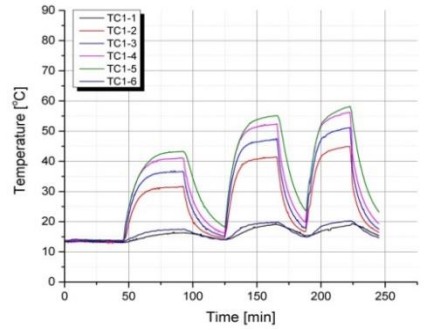

(a) TC1

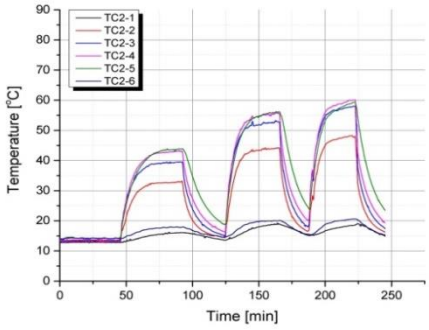

(b) TC2

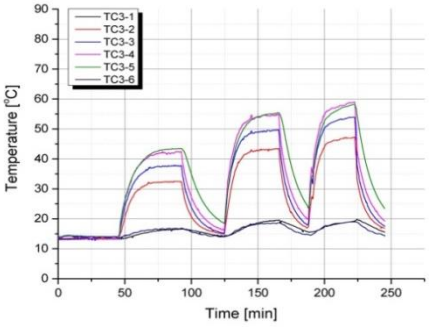

(c) TC3

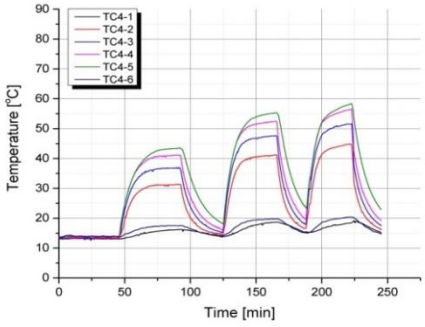

(d) TC4

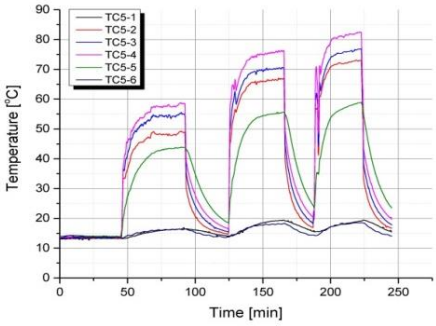

(e) TC5

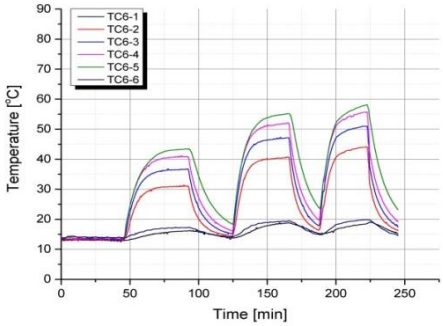

(f) TC6

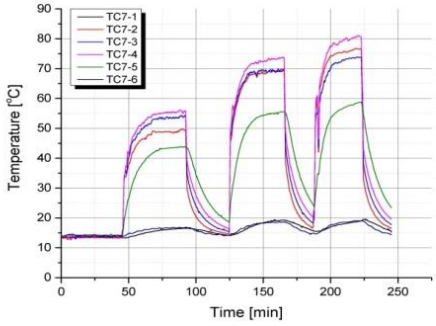

(g) TC7

FIGURE 15 Temperature Distributions for Each TC Set for the Second Water Irradiation: A Rastered Beam at 6, 10, and 12 kW. TC5 and TC7 were heated up directly by the beam and do not represent the water temperatures.

beam results. With an unrastered, concentrated beam (first two bumps at 3 and 6 kW), water is hottest at the beam height (TCx-4 and TCx-5 on each plot), while, with rastering, the temperature distributions evened out on the vertical (Z) axis with a gradient pointing towards the top. The exceptions are TCx-1s because the rastering does not reach all the way to the bottom and TCx-6s due to being in the air, on top of the target solution (in this case, water). Both figures demonstrate that there is not much variation horizontally (X and Y axis) and temperature distributions look pretty uniform throughout the TC sets, with the exception of TC5 and TC7. An important note to make here is that because of their locations (in front of the target), TC5 and TC7 sets were getting hit directly by the beam and they do not represent the actual temperatures of the surrounding target solution.

3.4 URANYL SULFATE IRRADIATIONS

As mentioned above, three experiments were performed with a 20 L uranyl-sulfate solution (140 g-U/L of DU). The experiments consisted of a short irradiation (approximately 1 hour after the steady state) followed by two long irradiations. Temperature distribution data sets for each experimental campaign are presented in Figures 16, 17, and 18. These data sets reveal very similar temperature characteristics to those seen in the water irradiations. The short irradiation at 10 kW shows that the maximum steady-state temperature at this power level is around 60°C (see Figure 16). It takes about 25–30 minutes to reach the thermal steady state after the beam is turned on. After the shutdown, pre-irradiation temperature levels are restored in about an hour. The first long irradiation with the uranyl-sulfate solution was done at 6, 10, 12, and 15 kW, increasing the beam power in steps (Figure 17), while the second long irradiation was performed at 6, 12, and 15 kW of beam power (Figure 18). These data sets also demonstrated the same temperature trends already known from the previous experiments. The maximum steady-state temperatures of 70°C were observed at 15 kW of beam power for both runs. Roughly 58% of the beam power is deposited in the target solution, which means that at 15 kW, the average power density of the target solution is about 15 x 0.58/20 = 0.435 kW/L. This is very close to the operating power density level of the SHINE subcritical system. Steady-state temperature levels for the first long irradiation with the uranyl-sulfate solution are summarized in Table 1. Again, TC5 and TC7 were getting struck directly by the beam and they do not correspond to the actual solution temperatures.

3.5 BUBBLE FORMATION AND BEHAVIOR

As described above, multiple cameras were used simultaneously to qualitatively observe the operation of the experiment and investigate the phenomena of bubble formation and transport during irradiation. Figure 19 shows a composite of representative images from the various cameras for steady-state conditions at 12 kW beam power. Due to the relatively poor resolution and magnification of the other cameras, only the primary camera was sufficient for quantitative image processing of bubble size and velocity. Even then, images of sufficient quality and contrast could only be obtained at several points near the upper liquid surface as well as a couple points at the beam centerline where lighting was adequate.

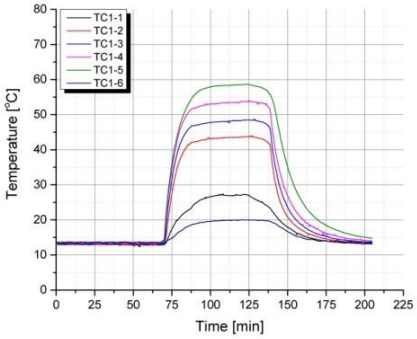

(a) TC1

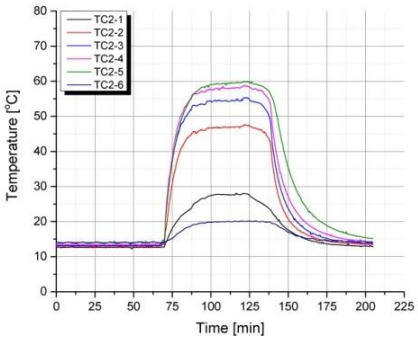

(b) TC2

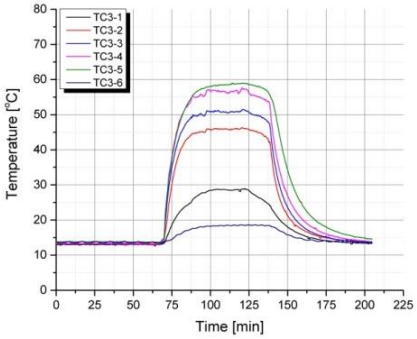

(c) TC3

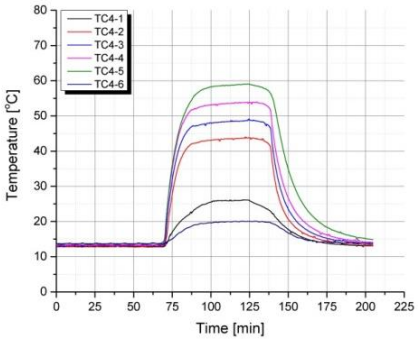

(d) TC4

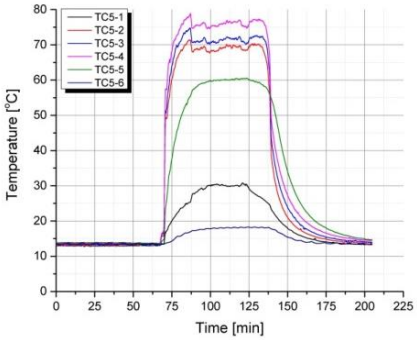

(e) TC5

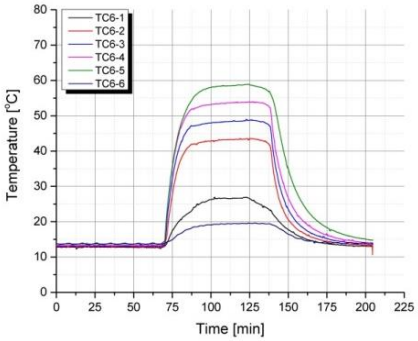

(f) TC6

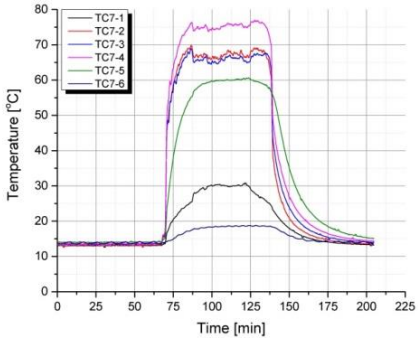

(g) TC7

FIGURE 16 Temperature Distributions for Each TC Set for the Short Uranyl Sulfate Irradiation at 10 kW of Beam Power. TC5 and TC7 are getting heated up directly by the beam.

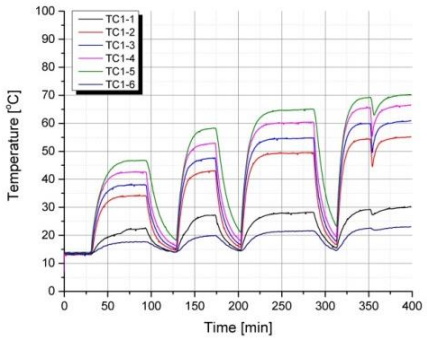

(a) TC1

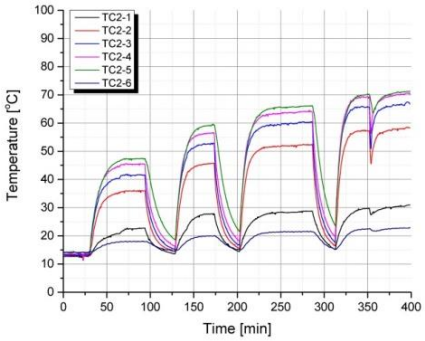

(b) TC2

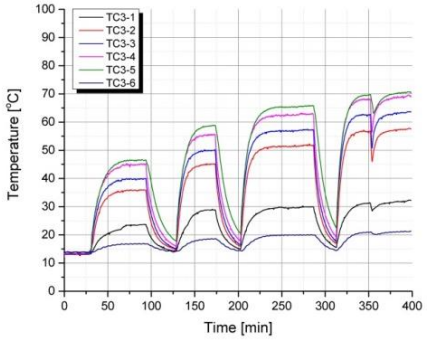

(c) TC3

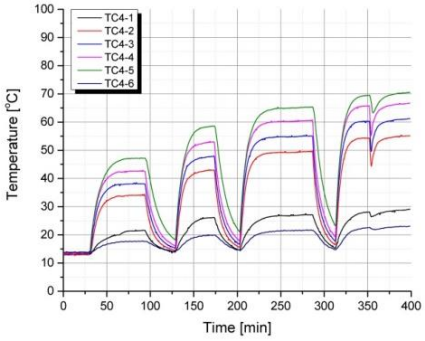

(d) TC4

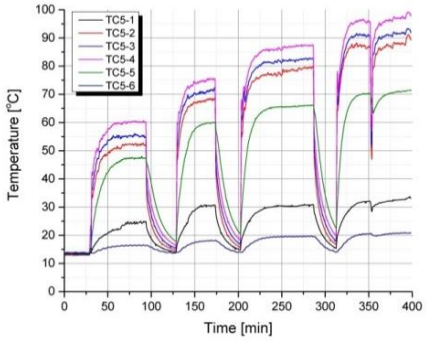

(e) TC5

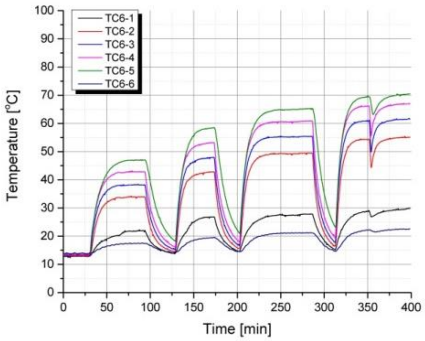

(f) TC6

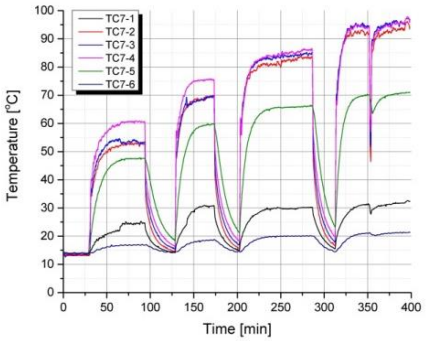

(g) TC7

FIGURE 17 Temperature Distribution Profiles for each TC Set for the First Long Irradiation with Uranyl Sulfate at 6, 10, 12, and 15 kW of Beam Powers. TC5 and TC7 are getting hit directly by the beam.

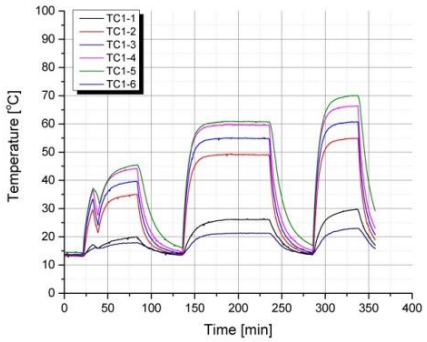

(a) TC1

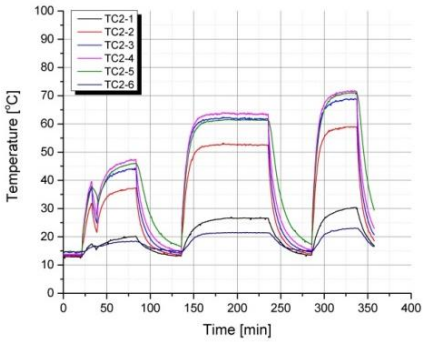

(b) TC2

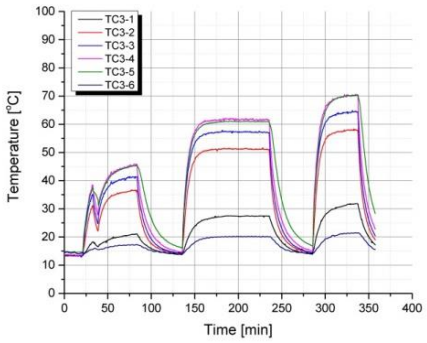

(c) TC3

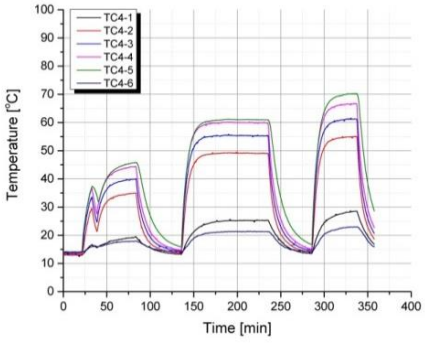

(d) TC4

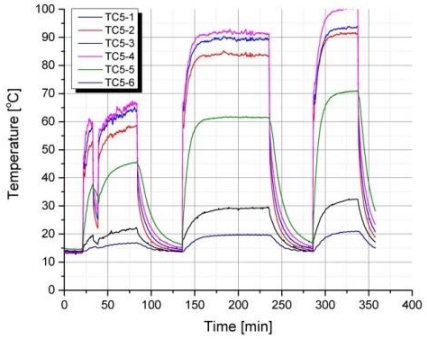

(e) TC5

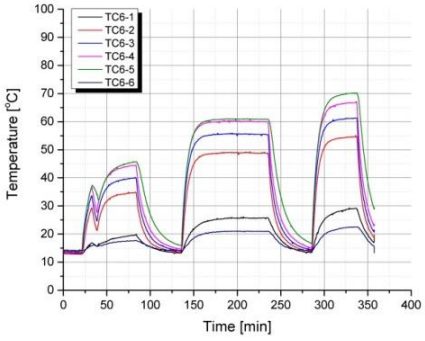

(f) TC6

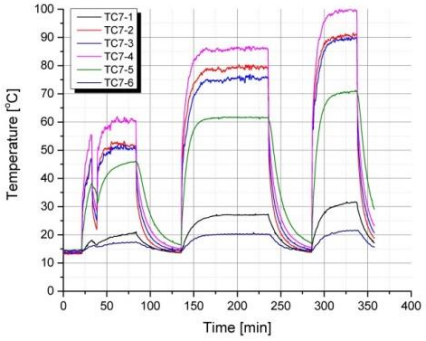

(g) TC7

FIGURE 18 Temperature Distribution Profiles for Each TC Set for the Second Long Irradiation with Uranyl Sulfate at 6, 12, and 15 kW of Beam Powers. TC5 and TC7 are getting hit directly by the beam.

TABLE 1 Steady-State Temperatures of Each TC for the First Long Irradiation with Uranyl Sulfate Solution

	TC1	TC2	TC3	TC4	TC5	TC6	TC7
				6 kW			
1	22.5	22.6	23.4	21.5	24.4	22	24.6
2	34.1	36	35.9	33.9	47.5	33.9	47.7
3	38	41.6	39.9	38.1	52.2	38.3	52.9
4	42.5	45.5	44.9	42.5	55.5	42.8	54
5	46.7	47.4	46.6	47.2	60.3	47.1	60.8
6	17.6	18	16.8	17.6	16.5	17.4	16.9
				10 kW			
1	27.1	27.8	28.9	26.2	30.5	26.8	30.7
2	42.8	45.6	45.1	43	60	42.8	59.7
3	47.5	52.5	50	47.8	68.4	47.8	69.4
4	52.9	56.4	55.5	53	71.6	53.2	69.9
5	58.2	59.2	58.7	58.5	75.7	58.5	75.6
6	19.9	19.9	18.6	19.9	18.2	19.5	18.7
				12 kW			
1	28.1	28.6	29.9	27.1	30.9	27.8	30.2
2	49.5	52.4	51.7	49.5	65.8	49.5	66
3	54.6	60.3	57.2	55	79.6	55.5	83.3
4	60.3	64.2	62.9	60.5	82.8	61	84.7
5	65	66	65.6	65.3	87.5	65.3	86.2
6	21.5	21.5	20	21.6	19.7	21.1	20.2
				15 kW			
1	30	30.5	32.1	28.8	32.8	29.9	32
2	55.1	58.1	57.6	55	71.3	55	71
3	60.8	66.5	63.7	61.1	88.3	61.6	93.8
4	66.5	70.2	69.2	66.5	91.9	67	95.3
5	70.2	71	70.8	70.5	97.5	70.3	96.4
6	22.9	22.8	21.1	22.9	20.8	22.6	21.3

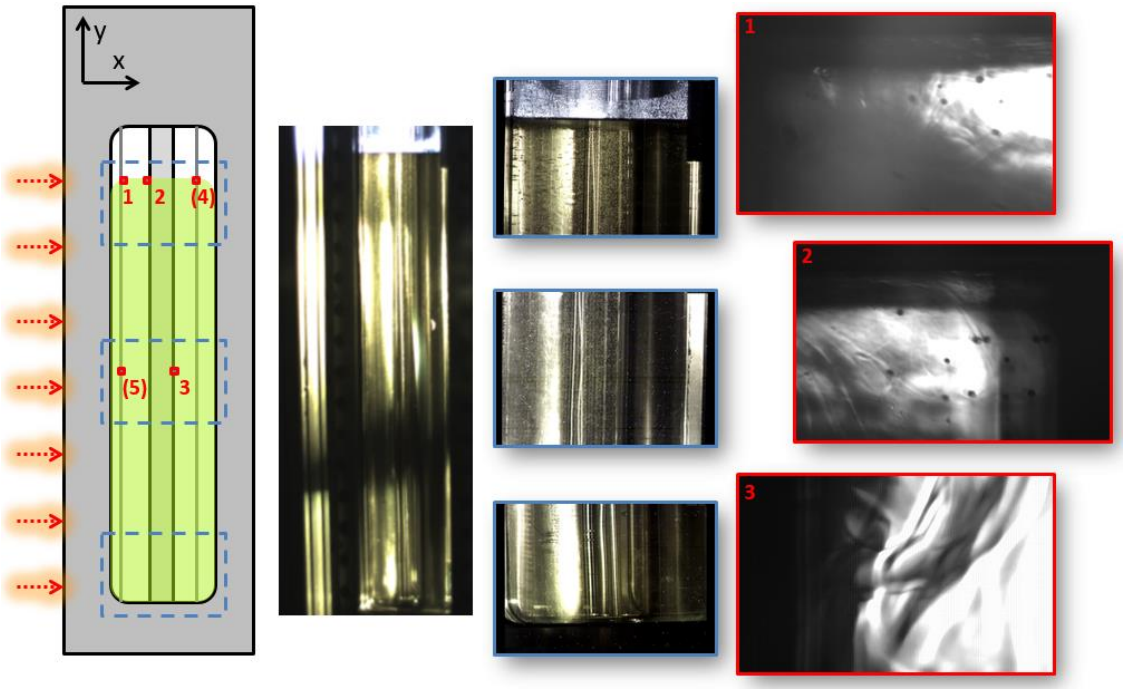

FIGURE 19 Composite of Images from the Various Cameras Showing Representative Snapshots of the Steady-State Flow Conditions at 12 kW Beam Power. The images at the far right in which bubbles appear as dark circles are from the primary camera which has a field of view of approximately 13 mm by 8 mm.

In general, it was found that the expected natural circulation loop with the flow going upward near the front surface (relative to the beam direction) and downward at the center cooling channel and beyond. The general flow pattern could be observed by noting refraction fronts due to local density variation similar to the technique used in shadowgraphy (see inset for position 3 in Figure 19). While such density striations aided in the observation of the bulk liquid flow, they unavoidably complicate bubble imaging by distorting bubble shape and focus. Despite this, the bubbles could be easily observed in the high magnification, primary camera images as dark circles. In the secondary cameras, the bubbles appear more as glints of reflected light due to the glancing angle of the camera and mirror orientation in this case. The bubbles appeared to be homogenously nucleated (in the solution as opposed to on surfaces) with the majority of visible bubbles found in the upper half of the domain and virtually none in the lower ~1/3 of the vessel.

Cherenkov radiation was seen when the electron beam from LINAC hit the target solution (Figure 20 (a), (b)). At the place where Cherenkov radiation was observed, its intensity was much stronger than that of the lighting from three 250 W LED stage spotlights. Since the scanning frequency of the electron beam did not synchronize with the capture speed of the cameras (frame rate), Cherenkov radiation only lit up a small area with a low scanning frequency in the videos captured by the cameras. It may be possible to eliminate the need for external lighting by synchronizing the scanning speed of the electron beam with the frame rate of the cameras. In our current experimental configuration, lighting from LED stage spotlights is absolutely necessary.

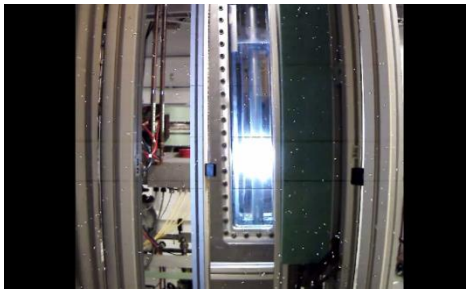

(a)

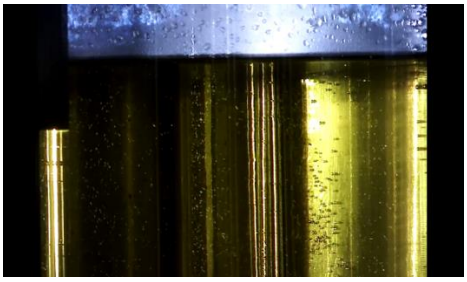

(d)

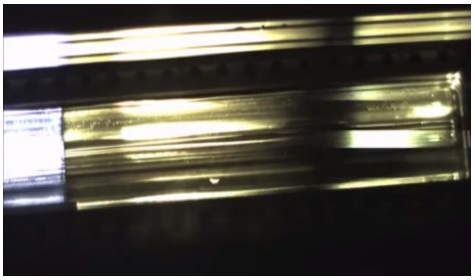

(b)

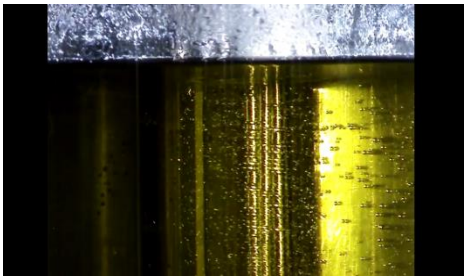

(e)

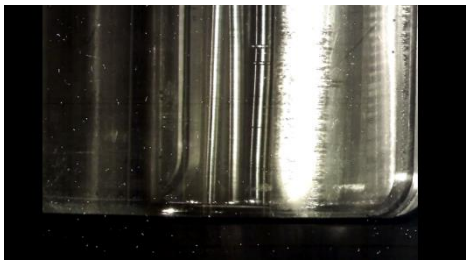

(c)

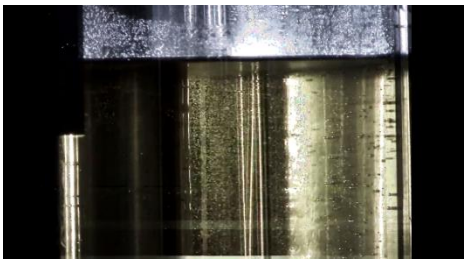

(f)

FIGURE 20 Some Videos Captured by the IP Cameras (videos can be watched directly by clicking them in MS Word 2013 on a PC or in MS Word 2011 on a Mac).

(a) Cherenkov radiation in water test. Video was captured by low resolution BNC camera. (https://www.youtube.com/watch?v=Vj5TiLs_LaE)

(b) Cherenkov radiation in uranyl sulfate solution. Video was captured by colored USB camera horizontally. (https://www.youtube.com/watch?v=UxZ40bHldw4)

(c) Bottom view of the solution at 15 KW beam power. Two thermal couples were "dancing slowly". Their vibration appeared as a sinusoidal wave. (https://www.youtube.com/watch?v=0hVcj7s_Kh8)

(d) Top view of the solution at 6 KW beam power. (https://www.youtube.com/watch?v=1P_m1nlfnqc)

(e) Top view of the solution at 12 KW beam power. (https://www.youtube.com/watch?v=meNm3ZFs0wY)

(f) Top view of the solution at 15 KW beam power. A thermal couple was "dancing" in the solution. (https://www.youtube.com/watch?v=5TjWLTmBo6s)

Large quantities of bubbles were seen in all the irradiations with different incoming beam power (6 KW, 12 KW, and 15 KW). Since (1) the uranyl-sulfate solution headspace was flushed with helium gas for about six hours before the experiments to purge air in the system and (2) the bubbles were created consistently during the long irradiation period, it is conceivable that the bubbles had not come from any air previously in the solution, but originated from the radiolysis of solution instead. The later data analysis from the gas collection system also supports this claim; a significant amount of hydrogen and oxygen were observed in the head space above the bubble chamber. From the visual observation of the IP cameras, one could notice that the bubbles started to show up at about 1/3 of the height of the bubble chamber and then they rose up to the surface. Bubble coalescence was not seen visually in the middle of the solution. Only a few isolated cases of coalescence were observed along the walls of the chamber where some bubbles were adhered. This observation is also confirmed by the sized distributions reported in the next section.

No foam was seen or built up at the surface or inside of the uranyl-sulfate solution (Figure 20 (d), (e), (f)). For all power levels tested and at all times, all the rising bubbles broke and released into the head space. About five minutes after the irradiation, the entrained gas was all released from the solution, and the solution returned to a clear state. Therefore, it is unlikely that bubble generation would produce any foam that could block any tube and transport lines in the future SHINE plant as had previously been considered to be a possible concern.

The bubble size at three different powers did not change dramatically. Instead, the number of bubbles increased noticeably according to the beam power. The flow patterns in the 6 kW case were more clearly in a transition to turbulence regime whereas the higher power cases (12 kW and 15 kW) exhibited more turbulent-like behavior (Figure 20 (d), (e), (f)).

The thermocouple closest to the beam was found to vibrate noticeably, particularly at the 12 kW and 15 kW conditions (Figure 20 (c), (f)). While this vibration appeared as a sinusoidal wave on the IP cameras (see video link for Figure 20 (c)), this was an artifact of the relatively long exposure time and rolling shutters on these cameras. From the USB 3.0 cameras the motion was more apparent as a single-mode bend vibration over the length of the tube. A set of images from the primary camera were taken at a vertical position at the beam height and focused on the vibrating thermocouple tube (position 5 in Figure 6) during the 12 kW conditions. Unfortunately, the period of the oscillation could not be clearly determined due to a substantial number of skipped frames in the set, but the magnitude of the vibration at the beam height was found to be approximately 2 mm in the imaging plane.

The advantage of using a telecentric lens system is that the focal plane can be scanned in and out in depth with no change in magnification. Thus, while the depth of field of the focal plane is rather small, any features that may not be fully in focus are still of the correct size. The ability to scan in the depth also made it possible to gain some qualitative insight into the variation of the flow in the transverse plane. From this effect, it was observed that the majority of bubbles were in the central region of the flow. Further, it was found that just in front of the central cooling channel, the flow was in the downward direction near the channel, but flowing upward near the side window. Unfortunately, there was no internal reference system to

determine the actual depth position of focus. Rather, the position of the focal plane was chosen so as to optimize the clarity of the features in the flow.

3.6 SIZE AND DISTRIBUTION

Quantitative scaling of the acquired images from the primary camera was done by taking an image of one of the thermocouple tubes with a known diameter of 1/8". The physical scale of the image was thus determined to be 6.7 microns/pixel making the overall image dimensions 12.9 mm by 8.0 mm. The ImageJ[1] software was used to identify and measure each individual bubble, taking care to not double count a given bubble in multiple frames. Conversely, when the same bubble is measured in successive frames such as is done for velocity estimation as presented in the next section, one can get an estimate of the uncertainty on the diameter measurement. On average, the uncertainty was found to be about ±5%. A representative bubble-size distribution for both the 6 kW and 12 kW power levels near the top of the liquid and just inside the center cooling channel (position 2) is shown in Figure 21. In both cases, the bubble size distribution seems to follow a normal distribution indicating no significant bubble coalescence is occurring in the system (when a log-normal distribution would be expected) and a dilute regime assumption should be valid.

The mean diameter in all cases is perhaps slightly smaller for the 6-kW condition with an overall mean of 205 microns compared to 267 microns for the 12-kW case (Table 2). If one assumes there is some significance to the difference, it is not clear if this is due to the increase in the average temperature of the solution or due to the increased gas production rate at the higher power deposition rate. While an estimate of the gas-volume fraction is unfortunately not feasible

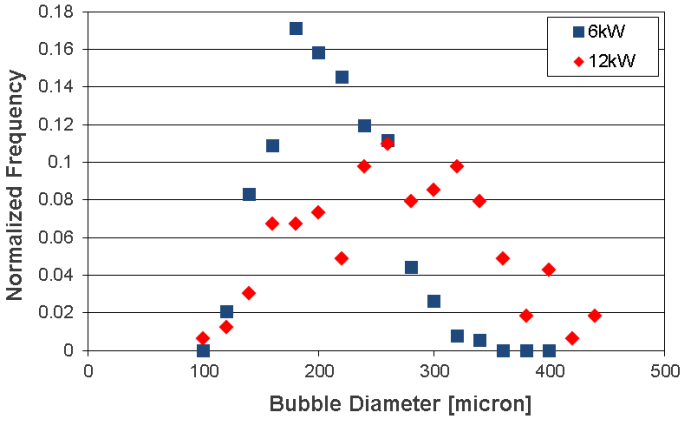

FIGURE 21 Bubble Size Distribution Near the Top of the Liquid Just Inside the Center Cooling Channel (position 2) for the 6 kW and 12 kW Power Settings

1 Imagej.nih.gov/ij/

TABLE 2 Summary of Mean Diameter Measured at Each Position for the Two Power Levels

	Beam Power	
Position	6 kW	12 kW
1	202 ± 41	280 ± 78
2	196 ± 45	258 ± 80
3	-	-
4	211 ± 52	-
d_{avg}	205	267
d_{stdev}	48	80
$N_{bubbles}$	1454	275

from these data, it was evident from the overall camera views that the number of bubbles increased somewhat with the beam-power level. Note that this is unfortunately not directly reflected in the number of bubbles that were counted for each case; rather, the opposite is seen. However, this was merely a result of more optimum lighting conditions in the 6 kW case (perhaps due to less severe thermally-induced density gradients) which gave a larger number of measureable bubbles, particularly at position 4. Due to experimental constraints, this position was only imaged for the 6 kW condition.

3.7 VELOCITY

Tracking of individual bubbles for estimation of x- and y-direction velocity components was readily done using the coordinates for the fit circle from successive frames. For estimation of the liquid velocity, only a single component could be determined for regions where the flow had a dominant directionality—such as at the top surface where the flow is almost completely in the x-direction or near the center cooling channel where the flow is downward. In such cases, the striations due to local density variations caused by temperature fluctuations could be tracked to extract the velocity of the propagating wave front. Velocity estimates were somewhat complicated by the fact that there were often skipped frames, though the camera software numbered the frames consecutively regardless, and the absolute timestamp of the frame was not retrievably saved to the file's metadata. In most cases, the number of skipped frames could be reliably estimated given that over the short range of the high magnification image (~10 mm) the velocity of a given feature did not vary tremendously and linearity could be assumed. Even so, this introduces some level of uncertainty in the velocity measurements and thus, they are given here as estimates only. In each case ~10 features (bubbles or density waves) were tracked over several frames and the results averaged. Table 3 gives a summary of the bubble velocity data, and Table 4 gives a summary of the liquid velocity estimations.

The downflow velocity of the 12 kW case is perhaps slightly greater than that at the lower power indicating somewhat enhanced natural convection. This is consistent with the larger

TABLE 3 Summary of Bubble Velocity Estimates Showing Magnitude with x and y Components in Parentheses

	Beam Power	
Position	6 kW	12 kW
1	-	4.3 ± 1.3 (1.0, 4.0)
2	-	5.0 ± 1.0 (0.8, 4.9)
3	-	-
4	2.3 ± 0.7 (1.4, 1.8)	-

TABLE 4 Summary of Bulk Liquid Velocity Estimates at the Various Measurement Positions. Relevant velocity component listed in parentheses. Note: 6 kW measurement at position 2 may be unreliable.

	Beam Power	
Position	6 kW	12 kW
1 (x)	-	0.8 ± 0.3
2 (x)	*5.3 ± 2.4*	2.0 ± 0.5
3 (y)	-2.1 ± 0.7	-2.7 ± 0.5
4	-	-

top-to-bottom temperature gradient observed in the temperature profiles with increasing beam power. While downflow on the front side of the center cooling channel was observed in both cases, the descending flow on the backside was clearly more prominent at both power levels observed. The bubble rise velocity near the top of the liquid is in the range of 4–5 cm/s for the 12 kW case and only ~2 cm/s for the 6 kW setting. This is perhaps due to the fact that the smaller bubble size in the 6 kW case also has a more significant horizontal component as it experiences greater drag by the bulk flow which is flowing outward (in the direction of the beam) along the top surface of the solution. It may also simply be due to local differences in the measurement locations.

It can also be noted from the images and videos that the flow in the low power case is clearly more in the laminar-turbulent transition regime whereas that for the 12 kW (and 15 kW) was clearly more turbulent in nature. This has implications for the heat transfer at the cooling walls and it will have an impact on the methods used for CFD modeling as discussed below.

3.8 GAS-LIQUID FLOW COUPLING

While some of the smallest bubbles were seen at times to follow the flow—with a few observed even flowing downward with the descending flow near the cooling channel—the majority of the bubbles were found rising to the liquid surface. It is not clear from the data whether the flow of the bubbles enhanced or diminished the natural circulation that developed in the system. Quantitatively, it did appear that there were more bubbles in the front half of the domain (on the beam side) where the flow is predominantly upward. A complicating factor to clear interpretation, however, is that increased bubble presence also leads to increased temperature gradients (due to a decrease in the effective thermal conductivity of the solution), thus compounding any effect on the natural circulation flow magnitude that might be present due to the flow of the bubbles themselves. Insight into this matter could be gained from future multiphase CFD studies in which it is more readily possible to separate the effect of the bubbles' flow from the effect of the thermally induced natural circulation flow patterns.

4 TREATMENT OF THE THERMOCOUPLE TEMPERATURE DATA

The solution was instrumented with seven six-channel thermocouples around the central cooling channel, as shown in Figure 22. Thermocouple channels 1–5 were in the solution and channel 6 was in the gas head space above the solution. In addition to these thermocouple assemblies, a thermocouple was affixed to the back of the primary containment wall and another was hanging in the secondary containment atmosphere to measure the atmosphere temperature. The arrangement of the thermocouple wires and central cooling channel are shown in Figure 22.

The cross-sectional area of the bubble chamber near the surface of the solution was calculated from the drawing dimensions as annotated in Figure 23 using the equations:

$A_{Primary} = 190.50\text{mm} \times 161.12\text{mm}$ (Primary volume cross-section, gray color in Figure 23)

$A_{Sides} = 2 \times 11.94\text{mm} \times 124.60\text{mm}$ (Side window cutouts, light blue color in Figure 23)

$A_{Channels} = -\frac{\pi}{4}\left((38.1\text{mm})^2 + 7 \times (3.18\text{mm})^2\right)$ (Remove area occupied by thermocouples and cooling channel, red color in Figure 23)

$$A_{Front} = 150\text{mm} \times 8.5\text{mm} - \left(\frac{(389.89\text{mm})^2}{2}\left[2\arcsin\left(\frac{150\text{mm}}{2\times389.89\text{mm}}\right) - \sin\left(2\arcsin\left(\frac{150\text{mm}}{2\times389.89\text{mm}}\right)\right)\right]\right)$$

(Front window cutout, blue-gray color in Figure 23)

$$A = A_{Primary} + A_{Sides} + A_{Channels} + A_{Front} = 33018.6\text{mm}^2$$

Which corresponds to a solution level change of 1 mm per 33.02 mL of volume change.

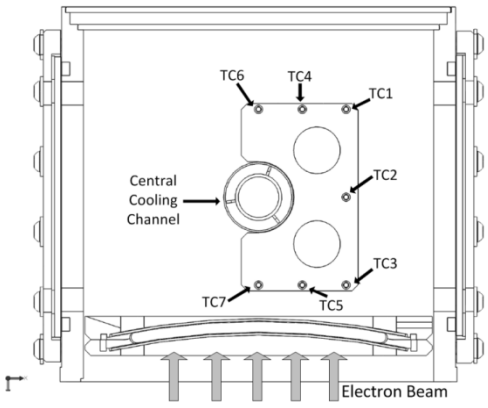

FIGURE 22 Cross Section of the Experiment Primary Containment Vessel

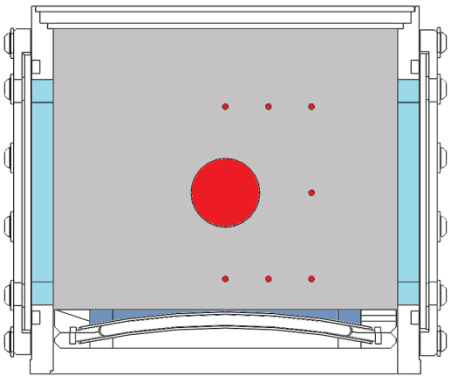

FIGURE 23 Areas Used to Calculate Total Cross-Section of the Wetted Surface

The temperature data used for this analysis were obtained from the ASCII output files 201412_114627.txt and 201412_174808.txt generated by the LabVIEW data acquisition software. The electron beam began impinging on the solution at 1240 seconds from the beginning of data acquisition. For the purpose of estimating the bulk solution temperature and corresponding height level change, the data were truncated to 501 minutes after the start of irradiation. Spurious data points generated by electromagnetic interference from the radiation field were filtered from the raw data using a point-by-point comparison of the data set. At each time t_n, the recorded value was compared to the data at t_{n-1} and t_{n+1}. If $(t_n - t_{n-1}) > 1$ and $(t_{n+1} - t_n) < -1$, the data point was deemed to be a spurious data point and replaced with the average of the values at t_{n-1} and t_{n+1}. Likewise, if $(t_n - t_{n-1}) < -1$ and $(t_{n+1} - t_n) > 1$, the data point was replaced with the average of the values at t_{n-1} and t_{n+1}. Using this methodology on the 1,489,008 points in the data set, 6,059 points were replaced with the average value of their neighbors (0.41% replacement). An example of the data from TC6-3 (TC6, channel 3, approximately in the middle of the solution) before and after filtering is shown in Figure 24 and Figure 25, respectively.

To estimate the aggregate thermal expansion of the fluid, the solution was divided into 125 voxels (25 zones in the horizontal x-y plane and 5 vertical positions in the solution), each assuming the temperature data shown in Figure 26. The assumed data points for the voxel calculation were based on the assumption that the heating profile was symmetric in the horizontal plane with an axis of symmetry about the central cooling channel. The T_{Body} assumption is representative of the actively cooled surfaces on the front and back of the primary chamber. Density data for 138 g-U/L from 20–80°C have been previously determined by experiment [11]. These data were extrapolated to a temperature range of 10–110°C to provide a set of data adequate for interpolation of density from the observed thermocouple data. These data were fitted to a 2nd order polynomial function to extend the temperature range. The fitting function was

$$\rho(T[°C])\left[\frac{\mathrm{g}}{\mathrm{mL}}\right] = -2.97619 \times 10^{-6} T[°C]^2 - 2.55952 \times 10^{-4} T[°C] + 1.20543$$

with an R^2 value of 0.999. Figure 27 shows the original data and the polynomial fit used for calculating volume changes in each of the 125 solution voxels.

The volume of the uranyl-sulfate solution at the start of the experiment (t = –20.066 min) was assumed to be 20 L with a mean temperature of 13.8°C and density of 1.201 g/mL. The equation used to calculate the volume-averaged temperature at each time step is:

$$\overline{T}(t) = \frac{1}{125}\sum_{i=1}^{5} 6T_{Body} + 4\left(T_{TC1,i}(t) + T_{TC2,i}(t) + T_{TC3,i}(t)\right) + 2\left(T_{TC4,i}(t) + T_{TC5,i}(t)\right) + T_{TC6,i}(t) + T_{TC7,i}(t)$$

with a corresponding solution height in millimeters of:

$$h(t) = \frac{20000}{30.02}\left(1 - \frac{\rho\left(\overline{T}(t)\right)}{\rho\left(\overline{T_0}\right)}\right) \text{ mm}$$

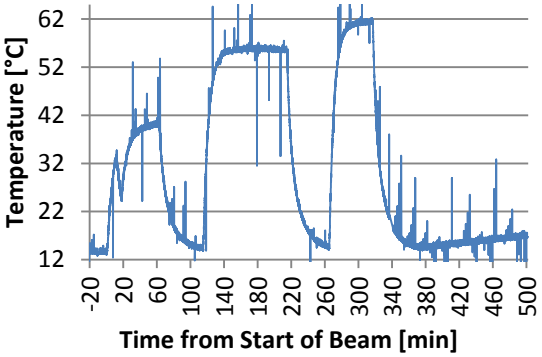

FIGURE 24 Raw Data Recorded on Thermocouple 6, Position 3

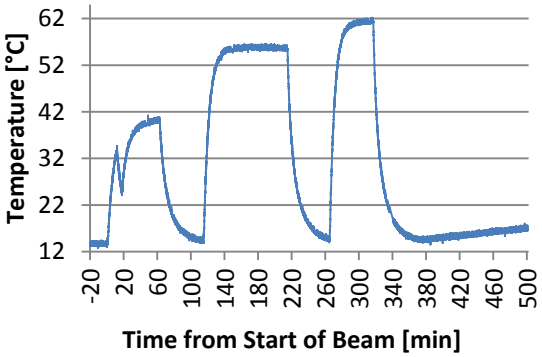

FIGURE 25 Filtered Data from Thermocouple 6, Position 3

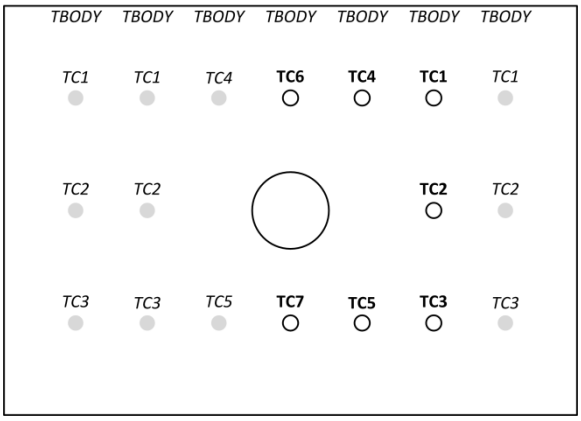

FIGURE 26 Arrangement of Thermocouple Data Used for Determining the Bulk Solution Temperature. Bold labels are recorded data and italic data are assumed data used to populate each of the 25 planar voxels for the calculation.

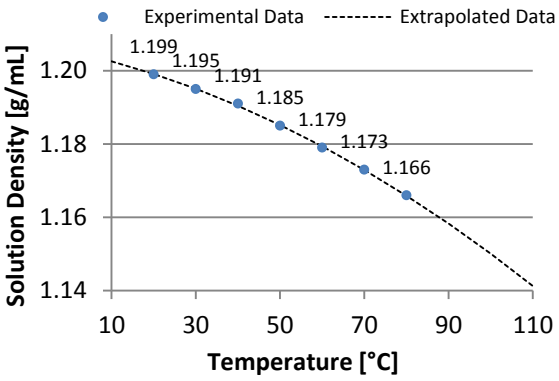

FIGURE 27 Density Data Used for Determining Thermal Expansion

The volume-averaged solution temperature and corresponding estimate of change in solution height due to thermal expansion are shown in Figure 28 and Figure 29, respectively.

From these data, the solution volume-averaged steady-state temperature for an electron beam power of 12 kW (0.6 kW/L, middle peak in Figure 28) over the time interval from 166 to 214 minutes was found to be 45.2±0.1°C. The sample irradiations at beam powers of 6 kW (first peak) and 15 kW (third peak) were not run long enough to calculate a steady-state volume-averaged temperature. In the absence of radiolytic gas bubble formation, the expansion of the solution due to heating should change the solution height from the initial condition by +6.79±0.02 mm.

The veracity of this simple solution bulk estimate was validated against the solution height measurements obtained from the camera data. The uranyl-sulfate solution height levels

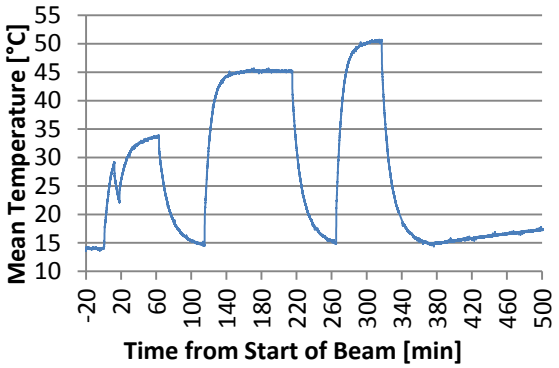

FIGURE 28 Volume-Averaged Solution Temperature during the Experimental Run

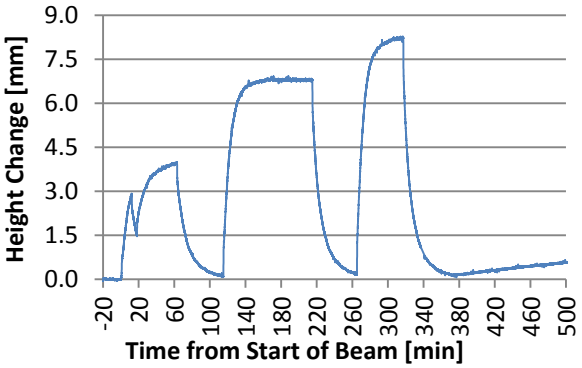

FIGURE 29 Thermocouple Estimate of Solution Level Change during the Experimental Run

were recorded at discrete time points during the irradiation. These data were converted to height change from the initial cold solution level as shown in Figure 30 and the bulk solution temperatures were estimated using the density data from Figure 31. The camera data indicate that the steady-state bulk solution temperature is 43.7±0.7°C and the change in solution height from the initial condition is 6.37±0.20 mm.

As a crude estimate of the solution bulk temperature, the voxel-based calculation is in fairly good agreement with the solution height-level data from the camera. However, the voxel model does not include the effect of void on the solution height. One would expect the thermocouple estimate of the solution temperature to be lower than that of the height-level data from the camera. This is most likely the result of (1) direct electron beam heating on thermocouples TC-5 and TC-7 and (2) neglecting the cooling effect of the central cooling channel on the uranyl-sulfate solution. A more detailed treatment of the bubble chamber using CFD simulations should yield a more accurate estimate of the bulk solution temperature.

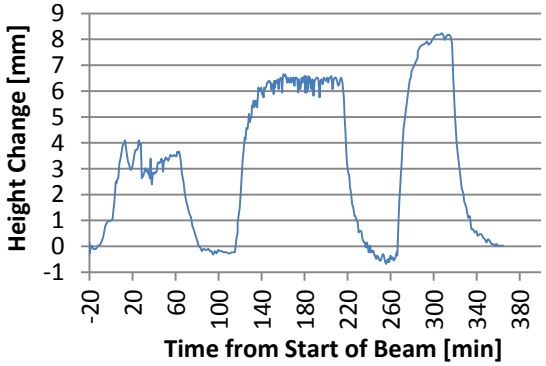

FIGURE 30 Camera Measurements of Solution Level Change during the Experimental Run

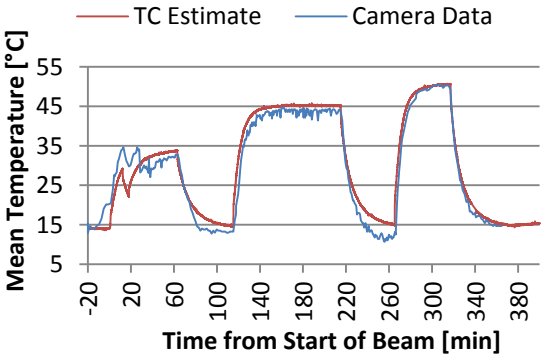

FIGURE 31 Comparison of Simple Voxel Estimate of Solution Bulk Temperature to Solution Height-Level Data Recorded by Camera

5 GAS CHROMATOGRAPH THERMAL CONDUCTIVITY DETECTOR DATA

The experiment was comprised of 20 L of uranyl-sulfate solution covered by a gas head space filled with helium. To prevent the accumulation of hydrogen, the head space was continually purged by a flow of helium gas at a rate of 30 mL/min. Gasses were swept from the headspace of the chamber and passed through a 2-liter condenser to reduce water vapor. Sweep gas then entered a sampling valve on the gas chromatograph. As gas flowed through the valve, it was periodically sampled for analysis. It was a once-through system which terminated with collection of the sweep gas. The pressure in the system was kept sub-atmospheric, between 970 and 980 mBar. Sample analysis was performed using a Shimadzu QP2010 gas chromatograph with a molecular sieve 5A column and thermal-conductivity detector (TCD). The detector was calibrated using five-point linear external standard calibrations with s>0.99. The reporting limit of the measurements is (a) H_2: 0.050 mole %, (b) N_2: 0.0100 mole %, and (c) O_2: 0.0100 mole %. The percent error of measurements is (a) H_2: 1.9 mole %, (b) N_2: 0.5 mole %, and (c) O_2: 2.6 mole %. The percent relative standard deviation of measurements is (a) H_2: 5.8 mole %, (b) N_2: 8.2 mole %, and (c) O_2: 8.3 mole %. The sampling rate of the GCMS was limited by the oven cool-down cycle of the instrument, which ranged from 9 to 19 minutes with a median sampling time of 11 minutes. Initial measurements were made of the gas stream prior to irradiation. The concentrations of hydrogen, oxygen and nitrogen were monitored. The nitrogen was monitored to account for atmospheric oxygen introduced through leaks in the system. Atmospheric oxygen was subtracted from the analytical results based on the measured nitrogen concentration using standard mass fractions of air (75.47% nitrogen and 23.20% oxygen in dry air). Neither the solution nor the headspace were sufficiently purged prior to the start of the experiment so residual atmospheric oxygen and nitrogen were present in the sweep gas stream. The mean solution temperature at the GCMS sample points are shown in Figure 32. The mean solution temperature is used to calculate the molar quantities of gases evolved from solution using the Ideal Gas Law.

Figure 33 shows the percent concentration of hydrogen and oxygen in the helium sweep gas at sampling time. The large headspace, condenser volume, and the continuous dilution of the sweep gas acted to smear the data. Concentrations of gases continually increased even through the solution cool down period between irradiation cycles due to the large mixing volumes present in the system. Hydrogen concentrations need to reach 0.05% to be detected. The first detection of hydrogen was at 137 minutes, which is 10 minutes after the beginning of the second irradiation. These were short irradiations, so solution chemistry and associated hydrogen and oxygen gas production rates were not allowed to reach a steady state. It would be expected for longer irradiations that hydrogen and oxygen concentrations would reach a steady-state maximum level in this experimental configuration since this is a once-through sweep gas system.

Figure 34 shows the μmoles of hydrogen and oxygen swept through the system between sampling times; it is another way to project the data shown in Figure 33. Figure 35 shows cumulative hydrogen and oxygen production throughout the experiment at sampling time. A longer irradiation should produce a curve beginning as an exponential function, then trending toward a horizontal asymptote as a function of increasing irradiation time.

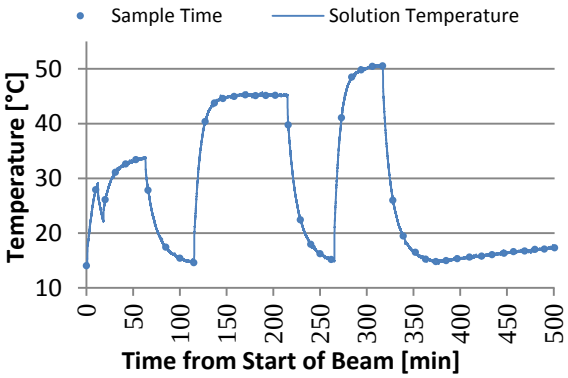

FIGURE 32 Mean Solution Temperature at the Times GCMS Samples were Taken

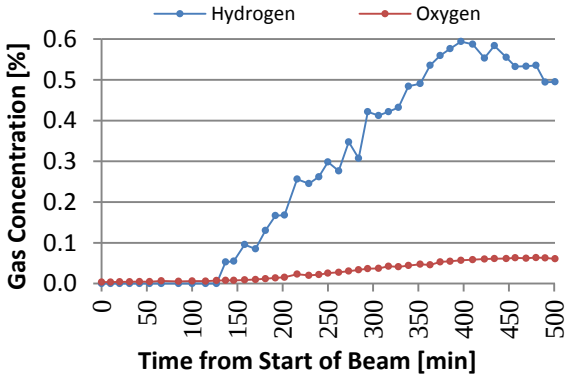

FIGURE 33 Hydrogen and Oxygen Molar Concentration Measured by the GCMS

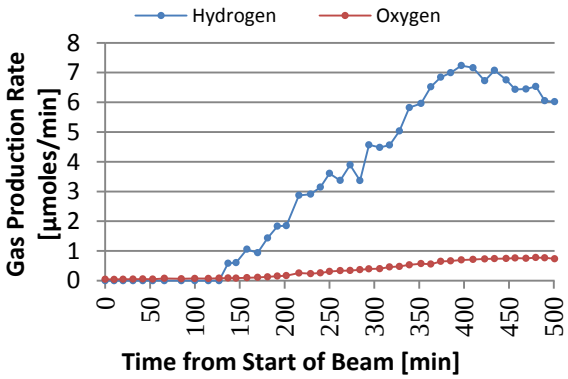

FIGURE 34 Hydrogen and Oxygen Production Estimates based on Sampled Gas Concentrations

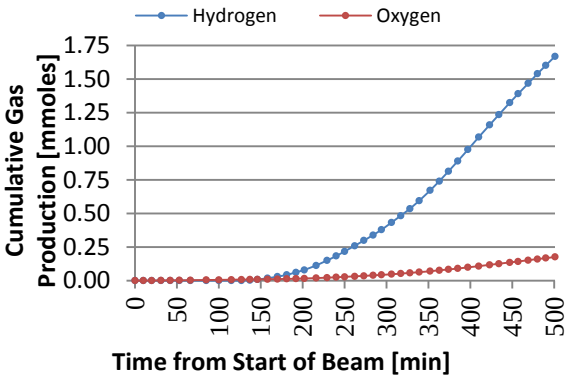

FIGURE 35 Integrated Production Quantities of Hydrogen and Oxygen during the Experiment

Figure 36 is the hydrogen and oxygen ratios both instantaneously at sampling time and cumulatively from the total production to time (*t*). One would expect the graphs to eventually approach a ratio of 2:1 hydrogen to oxygen as the uranyl sulfate approached the steady-state condition for radiolytic gas production.

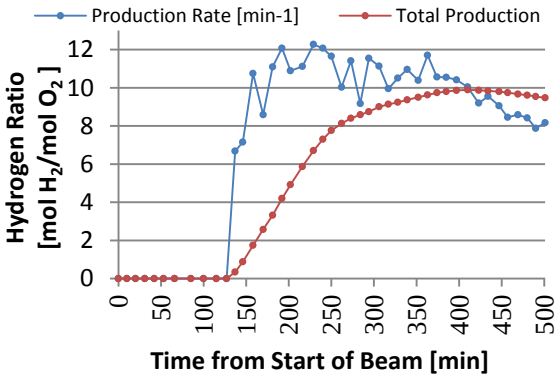

FIGURE 36 Ratios of Hydrogen to Oxygen Production for Sampled Concentration and Time-Integrated Gas Production

6 COMPARISON WITH CALCULATIONS

6.1 MCNP6 CALCULATIONS

The beam-profile distribution with a rastered beam was measured experimentally after completing the bubble formation study experiments. This was achieved by exposing a Plexiglas sheet with the electron beam for a short period of time (several seconds). The resulting darkened pattern on the sheet was then scanned and the beam distribution profile was obtained. This profile was later incorporated in an MCNP[2]6 model to simulate power deposition distribution in the target solution with a more realistic rastered beam. The electron flux distribution in the XZ plane (beam is traveling along the Y axis in this geometry) just behind the input window was obtained from MCNP6 modeling and is presented in Figure 37. This mimics the electron beam profile of the realistic rastered beam.

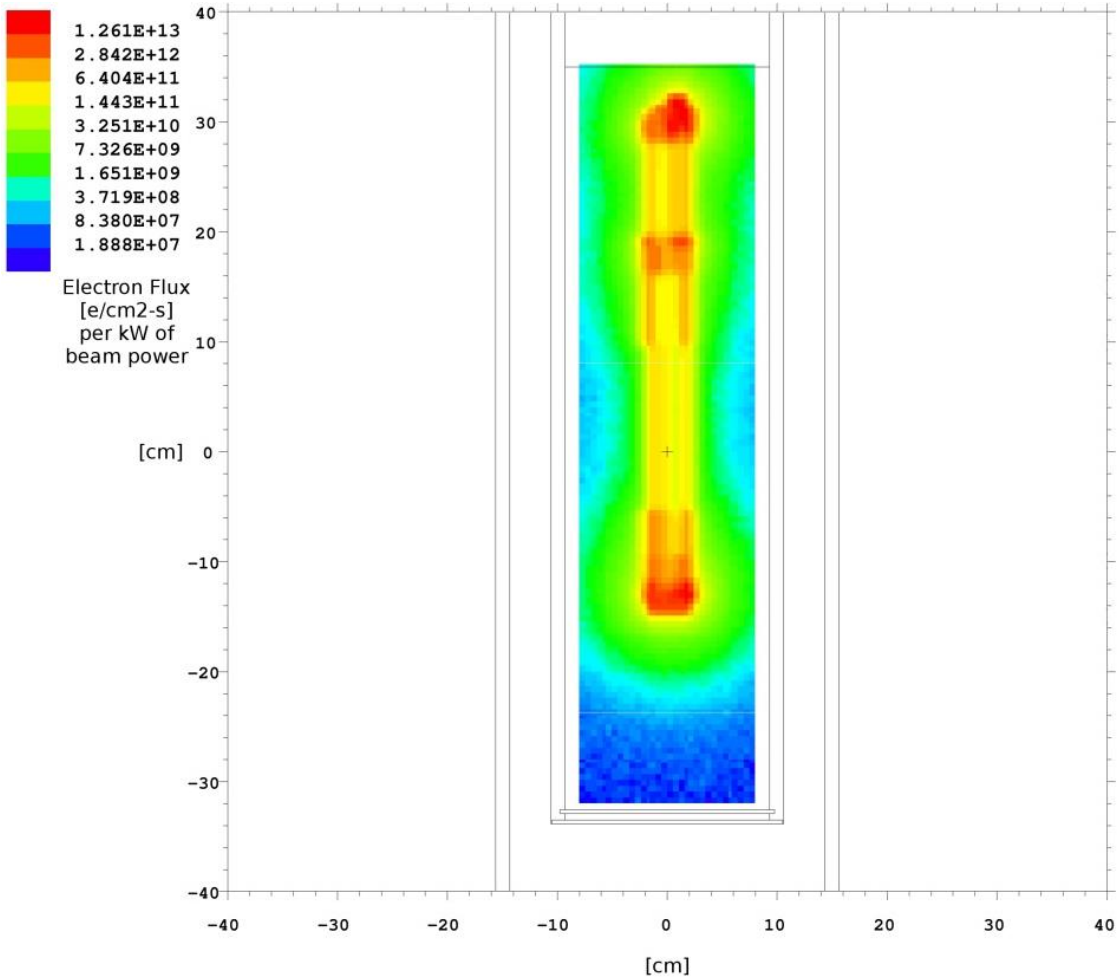

FIGURE 37 Electron Flux in XZ Plane Mimicking the Profile of the Experimental Rastered Beam. This is the result of MCNP6 modeling.

2 Monte Carlo N-Particle Transport code

Based on this beam profile, 3D total power distributions were obtained from MCNP6 for a 35 MeV electron beam. A 3D mesh with a voxel size of 5 mm x 5 mm x 5 mm was set up over the primary target chamber volume and total power deposition density was tallied for each voxel (type 3 mesh tally). XY, YZ and XZ profiles of this distribution are shown in Figure 38. The units are given in kW/cm^3 per kW of incident beam power. According to these results, the peak power density in the solution reaches up to 10 W/cm^3 per kW. These results also show that the power deposition along the beam axis is quite uniform. This is consistent with the observed experimental temperature data.

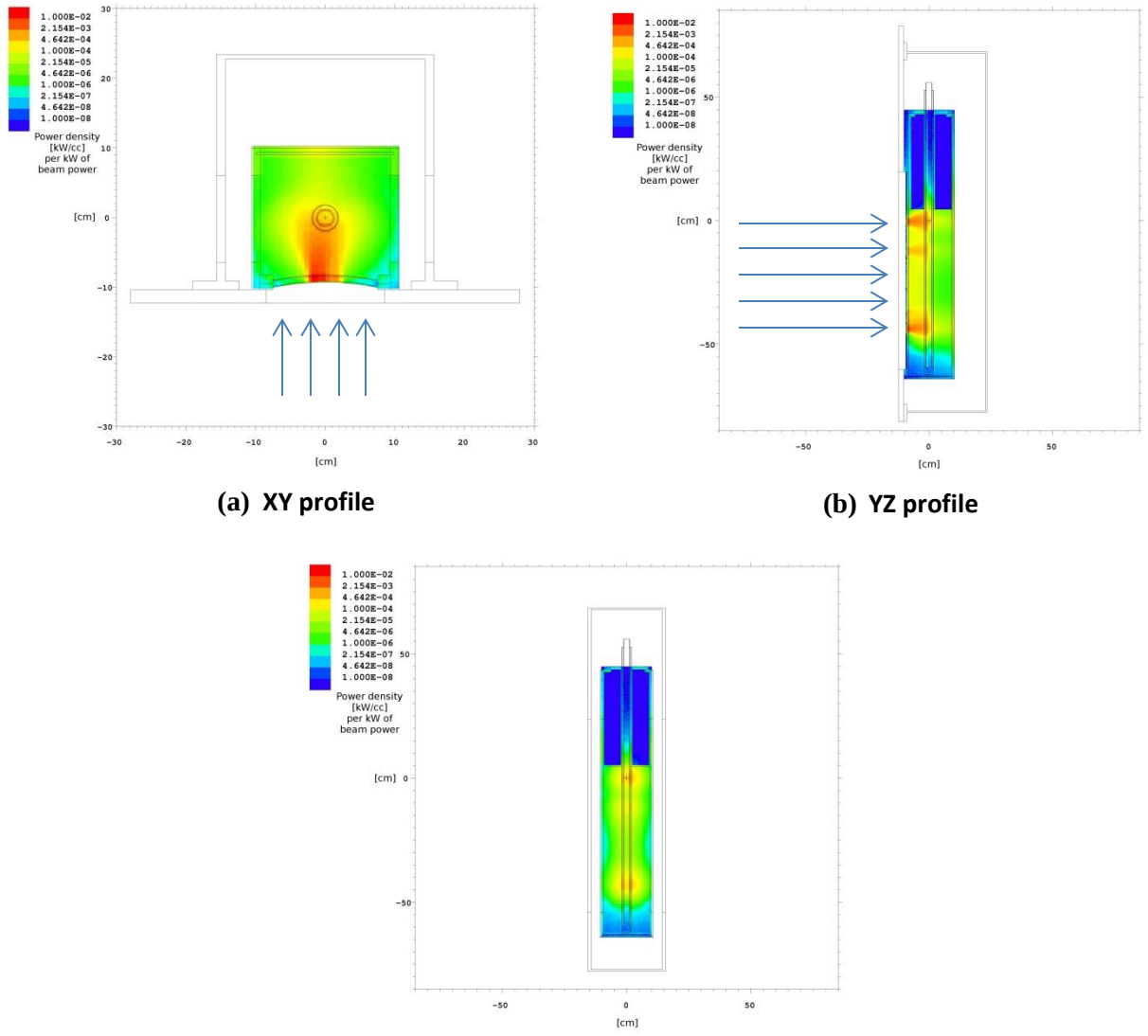

(a) XY profile

(b) YZ profile

(c) XZ profile

FIGURE 38 Total Power Deposition Profiles Modeled by MCNP6: (a) – XY Plane, (b) – YZ Plane, (c) – XZ Plane. Blue arrows illustrate the beam direction. Units are [kW/cm^3] per kW of beam power.

The total powers deposited in each cell of the target geometry were also calculated and are given in Figure 39. The plot shows that about 58% of the beam is deposited in the uranyl-sulfate solution. At 15 kW of beam power this amounts to 8.7 kW, which in turn means 0.435 kW/L of average power density. This is very close to the designed operating power density level of the SHINE subcritical assembly. Summing fractional deposited powers over all the cells gives about 86.3% of the initial beam power. The remaining 13.7% is irradiated away by the bremsstrahlung photons.

6.2 CFD CALCULATIONS

Initial thermal hydraulic CFD analyses were performed on the process fluid in a prototypic bubble chamber to determine the temperature distribution in the fluid. The purpose of these analyses was to provide guidance for the design of the cooling system for the bubble chamber. Design criteria for the cooling system were based on the avoidance of boiling in the process fluid. Two independent CFD analyses were performed using different methodologies that resulted in significantly different conclusions. A transient model using more complicated multiphase and turbulence treatment gave a modest temperature rise while a more significant temperature rise was obtained from the steady-state, single-phase model using averaged turbulence. The latter was used for sizing of the cooling system to provide the most conservative value for design purposes. The results of these analyses were described previously.[3]

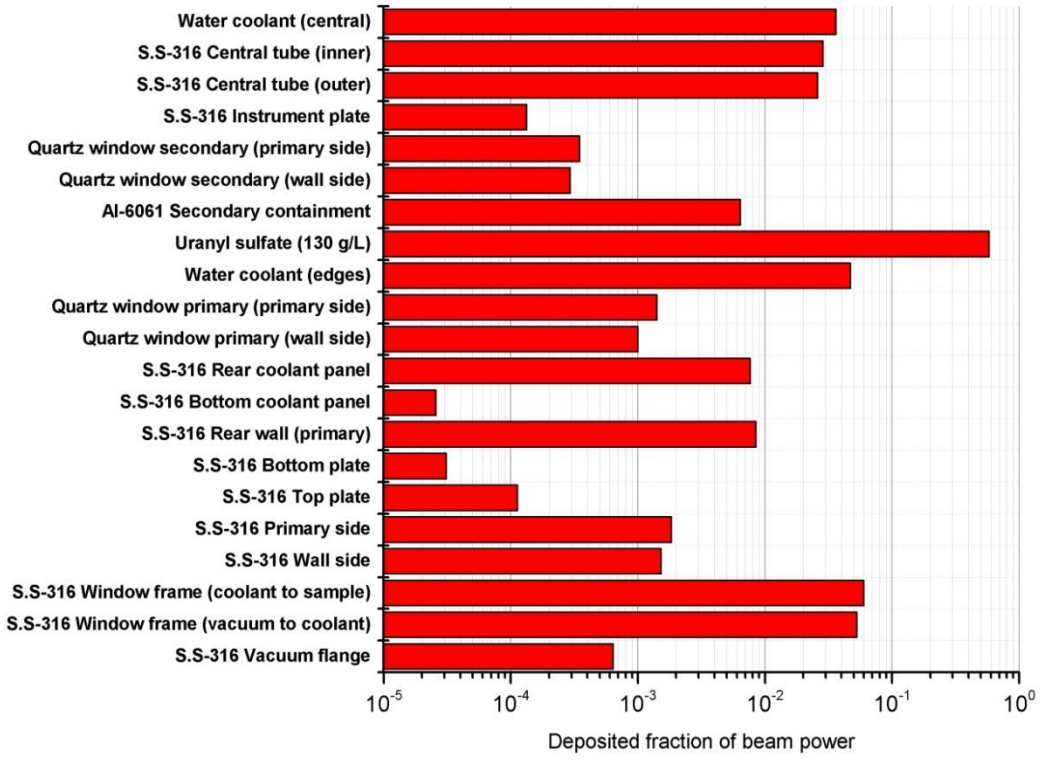

FIGURE 39 Fractional Power Depositions in Each Cell of the Target Assembly. Modeled with MCNP6 for a 35 MeV rastered beam.

Further thermal hydraulic analyses are required to simulate the actual geometry and experimental conditions and understand the discrepancies between the results in the previous two analyses. Differences in the assumed heat generation distribution, boundary conditions, and turbulence models are likely to account for these discrepancies. Also, there is now an opportunity to validate the CFD modeling based on temperature measurements that were taken during the bubble chamber experiment.

We plan to perform a parametric investigation, using the actual bubble-chamber geometry, including the central cooling channel, and applying both CFD analysis methodologies, to determine the sensitivity of the temperature distribution in the fluid to the assumed inputs of heat generation, wall temperatures, bubble characteristics, and turbulence. Evaluation of these results should provide a better understanding of the physical phenomena of importance for accurate prediction that give rise to the differences between the results of the two analyses. Further, based on field measurements taken during the bubble experiment, an accurate CFD simulation can be meaningfully compared to the measured temperature distribution in the process fluid. It is anticipated that the result of this analysis work will be a well-validated CFD model that will reliably predict the thermal hydraulic performance of the process fluid during irradiation. Such a model will enable additional exploration outside the space covered by the set of experiments (e.g., effect of central cooling channel on overall cooling and potential flow pattern disruption).

7 CONCLUSIONS

Although the upcoming analysis of the data will provide a comprehensive set of conclusions, the following conclusions can be reached at this point.

- Bubble formation occurs due to the homogeneous nucleation in the solution with the majority of bubbles in the upper half of the liquid and virtually none in the lower third.

- The mean bubble sizes found in the systems are quite small—significantly less than 1 mm, in the range of 200–300 microns in all cases—even at the top of the liquid where the bubble size would be expected to be at its largest.

- Bubble size follows a normal distribution indicating no significant coalescence is occurring in the system and a dilute regime assumption should be valid.

- The majority of the bubbles rise to the surface and are not recirculated or held up in solution beyond the time it takes for them to rise to the top.

- No foam was seen or built up on the surface or inside of the solution for any of the conditions tested.

- As the electron beam power increases, the sizes of the bubbles does not increase significantly. However, the number of bubbles increases noticeably.

- Flow patterns in the 6 kW case are more clearly in a transition to turbulence regime, whereas the higher power cases exhibit more turbulent-like behavior.

8 REFERENCES

1. Pitas, K.M., G.R. Piefer, R.V. Bynum, E.N. Van Abel, J. Driscoll, T.R. Mackie, and R.F. Radel, "*SHINE: Technology and Progress*," Proceedings of the Mo-99 2013 Topical Meeting on Molybdenum-99 Technological Development, April 1–5, 2013, Chicago IL, http://mo99.ne.anl.gov/2013/pdfs/Mo99%202013%20Web%20Papers/S6-P2_Pitas_Paper.pdf.

2. Pitas, K., "*The SHINE Path to a Reliable Domestic Supply of Mo-99*," Proceedings of the Mo-99 2014 Topical Meeting on Molybdenum-99 Technological Development, June 24–27, 2014, Washington, D.C., http://mo99.ne.anl.gov/2014/pdfs/presentations/S10P2%20Presentation%20Pitas.pdf.

3. Chemerisov, S., R. Gromov, V. Makarashvili, T. Heltemes, Z. Sun, K. Wardle, J. Bailey, K. Quigley, D. Stepinski, and G. Vandegrift, "*Design and Construction of Experiment for Direct Electron Irradiation of a Uranyl Sulfate Solution: Bubble Formation and Thermal Hydraulics Studies*," ANL/CSE-14/29, Argonne National Laboratory, in press.

4. Chemerisov, S., R. Gromov, V. Makarashvili, T. Heltemes, Z. Sun, K. Wardle, J. Bailey, D. Stepinski, and G. Vandegrift, "*Experimental setup for direct electron irradiation of the uranyl sulfate solution: bubble formation and thermal hydraulics studies*," Proceedings of the Mo-99 2014 Topical Meeting on Molybdenum-99 Technological Development, June 24–27, 2014, Washington, D.C., http://mo99.ne.anl.gov/2014/pdfs/papers/S9P10%20Paper%20Chemersiov.pdf.

5. Chemerisov, S., A.J. Youker, A. Hebden, N. Smith, P. Tkac, C.D. Jonah, J. Bailey, J. Krebs, V. Makarashvili, B. Micklich, M. Kalensky, S. Zaijing, R. Gromov, and G.F. Vandegrift, "*Development of the Mini-SHINE/MIPS Experiments*," Proceedings of the Mo-99 2013 Topical Meeting on Molybdenum-99 Technological Development, April 1–5, 2013, Chicago, IL, http://mo99.ne.anl.gov/2013/pdfs/Mo99%202013%20Web%20Papers/S11-P3_Chemerisov_Paper.pdf.

6. Youker, A.J., J.F. Krebs, M. Kalensky, P. Tkac, D. Rotsch, T. Heltemes, D.C. Stepinski, J.P. Byrnes, J.L. Jerden, W.L. Ebert, C. Pereira, M.J. Steindler, D.L. Bowers, S. Zaijing, S.D. Chemerisov, and G.F. Vandegrift, "*Overview: Argonne Assistance in Developing SHINE Production of Mo-99*," Proceedings of the Mo-99 2014 Topical Meeting on Molybdenum-99 Technological Development, June 24–27, 2014, Washington, D.C., http://mo99.ne.anl.gov/2014/pdfs/papers/S10P3%20Paper%20Youker.pdf.

7. Rotsch, D.A., A.J. Youker, P. Tkac, D.C. Stepinski, J.F. Krebs, V. Makarashvili, M. Kalensky, Z. Sun, T.A. Heltemes, J.F. Schneider, A.S. Hebden, J.P. Byrnes, L. Hafenrichter, K.A. Wesolowski, S.D. Chemerisov, and G.F. Vandegrift, "*Chemical Processing of mini-SHINE Target Solutions for Recovery and Purification of Mo-99*," Proceedings of the Mo-99 2014 Topical Meeting on Molybdenum-99 Technological Development, June 24–27, 2014, Washington, D.C., http://mo99.ne.anl.gov/2014/pdfs/papers/S9P8%20Paper%20Rotsch.pdf.

8. "Fluid Fuel Reactors," 979 pages, Addison-Wesley, 1958, Chapter 3, Properties of Aqueous Fuel Solutions, http://moltensalt.org.s3-website-us-east-1.amazonaws.com/references/static/downloads/pdf/.

9. Wren, J.C., "Steady-State Radiolysis: Effects of Dissolved Additives," Chapter 22, *Nuclear Energy and the Environment*, ACS Symposium Series 1046, eds., Chien M. Wei and Bruce J. Mincher, American Chemical Society, Washington, D.C. (2010).

10. Sun, Z., K. Wardle, K. Quigley, R. Gromov, A.J. Youker, V. Makarashvili, D. Stepinski, S. Chemerisov, and G.F. Vandegrift, "*Micro-Bubble Experiments at the Van de Graaff Accelerator*," ANL/NE-15/2, February 2015, http://www.ipd.anl.gov/anlpubs/2015/05/113420.pdf.

Nuclear Engineering Division
Argonne National Laboratory
9700 South Cass Avenue, Bldg. 205
Argonne, IL 60439-4854

www.anl.gov